https://doi.org/10.5194/egusphere-2026-4334
Preprint. Discussion started: 18 August 2026

Measurement report: Long-term 2D MAX-DOAS observations of HONO vertical distributions in a rice–wheat rotation agricultural region in Shouxian, China

Weiwei Hu[1,2], Ang Li[1], Zhaokun Hu[1], Junli Jin[3], Chaonan Lv[1,2], Hongmei Ren[4], Hairong Zhang[5], Jiangman Xu[6], and Min Qin[1]

[1]Hefei Institutes of Physical Science, Chinese Academy of Sciences, Hefei 230031, China
[2]University of Science and Technology of China, Hefei 230026, China
[3]China Meteorological Administration Meteorological Observation Centre, Beijing 100081, China
[4]School of Physics and Electronic Information, Anhui Normal University, Wuhu 241000, China
[5]Cixi Branch of Ningbo Municipal Bureau of Ecology and Environment, Cixi 315300, China
[6]Anhui Water Conservancy Technical College, Hefei 231603, China

Correspondence to: Ang Li (angli@aiofm.ac.cn)

Abstract. Nitrous acid (HONO) photolysis is an important source of hydroxyl radicals (OH) in the atmospheric boundary layer, but long-term observations of HONO vertical distributions and their responses to agricultural activities remain limited. We conducted nearly 2 years (2022–2023) of two-dimensional multi-axis differential optical absorption spectroscopy (2D MAX-DOAS) observations in a rice–wheat rotation region in Shouxian, China. Retrieval reliability and stability were assessed through an intercomparison between two synchronized systems, spectral fit quality, degrees of freedom for signal (DOFS), and averaging-kernel analysis. Meteorological data, farming records, backward trajectories, potential source contribution function (PSCF) analysis, and Tropospheric Ultraviolet and Visible (TUV) calculations were integrated to investigate HONO variability, fertilization effects, and potential OH production. HONO was concentrated below 0.5 km, with morning and late-afternoon peaks and a noon minimum. Seasonal means followed the order winter > autumn > spring > summer. In spring and summer, near-surface HONO decreased toward midday, whereas HONO increased aloft, suggesting possible radiation-associated replenishment in elevated layers. During the 10 d following fertilization on 15 March 2023, HONO concentrations at 0.05, 0.20, and 0.50 km increased by factors of 5.3, 3.7, and 2.5, respectively, relative to the preceding 10 d. Near-site PSCF values suggested local and short-range agricultural influences. At 0.05 km, potential OH production from HONO photolysis increased after fertilization by 710 % under clear-sky conditions and by 86 % under cloudy conditions. These findings demonstrate the importance of resolving HONO vertical structure and agricultural-event responses when evaluating its photochemical relevance in agricultural regions.

1 Introduction

Nitrous acid (HONO) is a short-lived reactive nitrogen species in the troposphere that plays an important role in atmospheric oxidation and photochemical pollution (Kleffmann, 2007; Spataro and Ianniello, 2014). It is rapidly photolyzed by near-

https://doi.org/10.5194/egusphere-2026-4334
Preprint. Discussion started: 18 August 2026

ultraviolet radiation to produce hydroxyl radicals (OH) and nitric oxide (NO), thereby providing an important primary source of OH, particularly in the early morning and polluted boundary layers (Alicke et al., 2003; Ye et al., 2023). The resulting radical chemistry can promote volatile organic compound (VOC) oxidation, ozone (O_3) formation, and the production of secondary inorganic and organic aerosols (Li et al., 2010; Li et al., 2011; Zhang et al., 2022):

$$\mathrm{HONO} + h\nu \rightarrow \cdot\mathrm{OH} + \mathrm{NO} \quad (1)$$

The gas-phase reaction of NO with OH is generally insufficient to account for observed daytime HONO concentrations (Li et al., 2012; Song et al., 2023). Additional sources have therefore been proposed, including heterogeneous NO_2 conversion on ground and aerosol surfaces, photolysis of deposited nitric acid and particulate nitrate, direct emissions, and other photochemical processes (Kleffmann, 2007; Song et al., 2023). Their relative contributions depend on solar radiation, NO_x abundance, surface properties and water films, aerosol loading, and boundary-layer dynamics, resulting in a HONO budget that varies markedly over time and across environmental conditions (Kleffmann, 2007; Stemmler et al., 2007; Spataro and Ianniello, 2014).

Agricultural soils may constitute an important yet poorly constrained source of HONO (Su et al., 2011; Wang et al., 2025). HONO can be released through soil nitrite accumulation and microbial nitrification and denitrification, with emissions controlled by soil moisture, temperature, pH, mineral nitrogen availability, and fertilization practices (Oswald et al., 2013; Bhattarai et al., 2021). Field flux measurements further show that fertilization can substantially enhance HONO emissions from croplands, although the magnitude and timing of the response vary with crop type, soil moisture, and growth stage (Laufs et al., 2017; Song et al., 2023). Emission inventories and global simulations likewise identify cropland soils and fertilizer application as important contributors to soil HONO emissions at regional and global scales, with potential effects on OH production, O_3 formation, air quality, and vegetation exposure (Gan et al., 2024; Wang et al., 2025).

Surface in situ measurements alone cannot readily separate soil and surface emissions from production aloft, vertical mixing, and regional transport (Wong et al., 2013; Xing et al., 2023). Vertically resolved observations have revealed strong near-surface HONO gradients, with profile shapes governed by boundary-layer stability, surface exchange, vertical transport, and chemical production aloft (VandenBoer et al., 2013; Xing et al., 2024). Long-term vertically resolved measurements are therefore essential for characterizing HONO vertical structure and its effective influence depth in agricultural regions and for better constraining its sources and photochemical impacts (Wang et al., 2019; Xing et al., 2024).

Two-dimensional multi-axis differential optical absorption spectroscopy (2D MAX-DOAS) exploits the elevation-angle-dependent light paths of scattered sunlight to retrieve vertical profiles of aerosol extinction and trace gases such as HONO and NO_2 (Hönninger et al., 2004; Frieß et al., 2006; Wang et al., 2017; Ryan et al., 2018; Wang et al., 2019). Jointly resolved HONO, NO_2, and aerosol profiles can provide insight into near-surface HONO formation and the vertical extent of surface-related processes (Wang et al., 2019; Xing et al., 2023). However, continuous multi-year HONO profile measurements remain scarce in representative rice–wheat rotation regions.

In this study, we use continuous 2D MAX-DOAS observations from 2022–2023 in a rice–wheat rotation agricultural region in Shouxian, within the Huai River Basin, to retrieve vertical profiles of HONO, NO_2, and aerosol extinction. Spectral fit

https://doi.org/10.5194/egusphere-2026-4334
Preprint. Discussion started: 18 August 2026

quality, averaging kernels, degrees of freedom for signal (DOFS), and an intercomparison between two collocated systems are used to assess retrieval quality, vertical sensitivity, and dataset reliability and stability. Meteorological observations, farming records, backward trajectories, and potential source contribution function (PSCF) analysis are then combined to characterize the vertical, diurnal, and seasonal variability of HONO and examine its lower-atmospheric response to a fertilization event in March 2023. Finally, the Tropospheric Ultraviolet and Visible (TUV) model is used to estimate potential OH production from HONO photolysis and evaluate its sensitivity to selected model inputs.

2 Methods and data

2.1 Measurement site and agricultural setting

The observation site is located near the Shouxian National Climate Observatory in Huainan, Anhui Province, China (32.44° N, 116.79° E; Fig. 1), where measurements were conducted for nearly 2 years. Situated in the Huai River Basin of eastern China, the site is surrounded mainly by contiguous cropland and rural settlements. The terrain is flat and open, with no major industrial point sources nearby and an unobstructed viewing sector suitable for long-term remote-sensing observations. Agricultural HONO fluxes have previously been measured in Shouxian and the broader Huai River Basin, but vertically resolved observations remain limited (Meng et al., 2022, 2024).

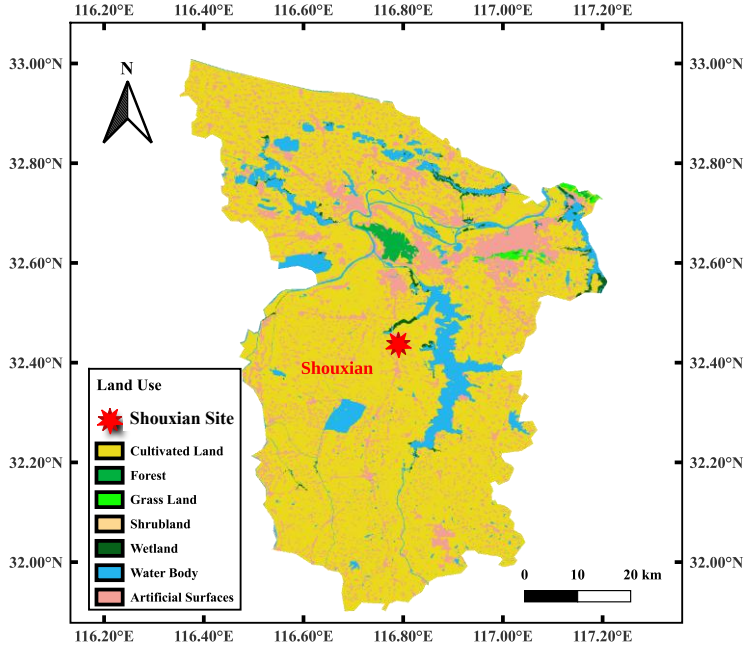

Figure 1. Land-cover types around Shouxian and the location of the 2D MAX-DOAS observation site. The map shows cultivated land, forest, grassland, shrubland, wetland, water bodies, and artificial surfaces derived from the 30 m GlobeLand30 product (Chen et al., 2015). The red star marks the observation site.

https://doi.org/10.5194/egusphere-2026-4334
Preprint. Discussion started: 18 August 2026

Shouxian is a representative agricultural region in the Huai River Basin, where winter wheat and rice are widely cultivated in rotation (Zhang et al., 2023). Based on published information, long-term field records from the Shouxian experimental site, and local farming practices, the typical crop-growth stages and major fertilization periods are summarized in Fig. 2. Winter wheat is generally sown in November of the preceding year, overwinters, and then progresses through green-up, jointing, booting, and harvest in May. Rice is generally sown or transplanted in June and progresses through tillering, jointing, heading and grain filling, and harvest around October. The main management periods include basal, green-up, and jointing fertilization for wheat and basal, tillering, and panicle fertilization for rice.

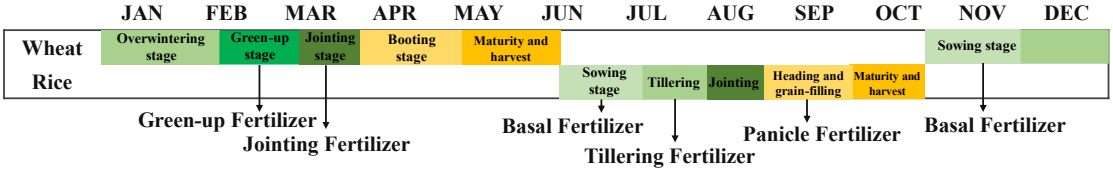

Figure 2. Typical winter wheat–rice rotation calendar and major fertilization windows in Shouxian. The upper and lower rows show the main growth stages of winter wheat and rice, respectively. Arrows indicate the approximate fertilization windows for basal, green-up, jointing, tillering, and panicle fertilization.

2.2 2D MAX-DOAS observations and profile retrievals

2.2.1 Instrumentation and measurement strategy

Two 2D MAX-DOAS systems, hereafter referred to as Shouxian and Shouxian5, were operated continuously at the site (Fig. 3). Each system comprised a telescope, an ultraviolet–visible spectrometer, a two-dimensional scanning platform, a quartz optical fibre, a temperature-control unit, and a control computer. Scattered-sunlight spectra were recorded at multiple elevation angles. Low-elevation observations sample longer effective light paths through the boundary layer and are therefore more sensitive to near-surface aerosols and trace gases (Hönninger et al., 2004).

The two instruments were installed on the same rooftop platform and operated with identical viewing geometry, comparable scan durations, and the same DOAS spectral fitting, PriAM profile retrieval, and quality-control procedures. As listed in Table 1, the viewing azimuth was defined relative to north, with 0° indicating due north. Both spectrometers were housed in temperature-controlled units maintained at 20 °C to minimize temperature-induced variations in wavelength stability and spectral response. Simultaneous observations were matched by measurement time to assess the consistency of HONO, NO_2, and aerosol retrievals from the two systems.

Table 1. Measurement specifications for the two synchronized 2D MAX-DOAS systems.

Instrument	Spectral range	Spectral resolution	Viewing azimuth	Elevation-angle sequence
Shouxian	296–460 nm	≈0.5 nm	18°	1°, 2°, 3°, 4°, 5°, 6°, 8°, 10°, 15°, 30°, 90°
Shouxian5	300–464 nm	≈0.5 nm	18°	1°, 2°, 3°, 4°, 5°, 6°, 8°, 10°, 15°, 30°, 90°

https://doi.org/10.5194/egusphere-2026-4334
Preprint. Discussion started: 18 August 2026

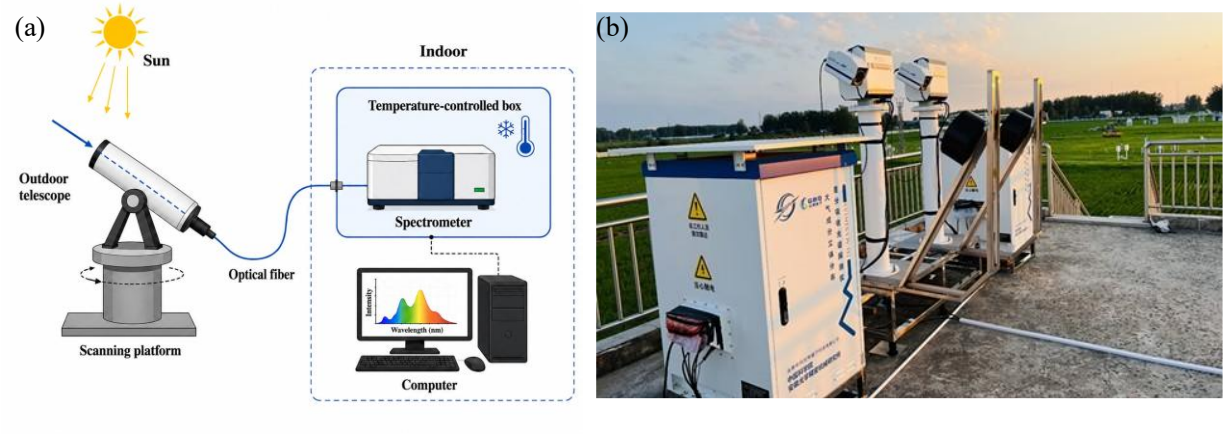

Figure 3. Configuration and field deployment of the 2D MAX-DOAS systems. (a) Schematic of the outdoor telescope unit, two-dimensional scanning platform, optical fibre, temperature-controlled spectrometer, and control computer. (b) Photograph of the two collocated 2D MAX-DOAS systems at the Shouxian observation site.

2.2.2 DOAS retrieval principles and spectral fitting settings

2D MAX-DOAS retrievals are based on the Beer–Lambert law and differential optical absorption spectroscopy (DOAS). DOAS separates the narrow-band absorption structures of trace gases from broadband extinction and instrumental effects associated with Rayleigh and Mie scattering, clouds, surface reflection, and the instrumental response (Hönninger et al., 2004; Platt and Stutz, 2008). Within a selected spectral fitting window, broadband structures are represented by a low-order polynomial, while the differential absorption features of multiple species are fitted simultaneously using least squares. The fitting yields the slant column density (SCD) of each absorber along the effective light path. The Beer–Lambert relationship can be written as

$$I(\lambda) = I_0(\lambda) \exp\left[-\sum_j \sigma_j(\lambda) \cdot \mathrm{SCD}_j - \tau_\mathrm{R}(\lambda) - \tau_\mathrm{M}(\lambda)\right] \quad (2)$$

where $I(\lambda)$ is the measured spectrum after atmospheric attenuation, $I_0(\lambda)$ is the reference spectrum, $\sigma_j(\lambda)$ is the absorption cross section of species j, and SCD_j is its slant column density along the effective light path. The terms $\tau_\mathrm{R}(\lambda)$ and $\tau_\mathrm{M}(\lambda)$ denote the optical depths associated with Rayleigh and Mie scattering, respectively. Taking the logarithm yields the optical-depth form commonly used in DOAS fitting:

$$\tau(\lambda) = -\ln\left[\frac{I(\lambda)}{I_0(\lambda)}\right] = \sum_j \sigma_j'(\lambda) \cdot \mathrm{SCD}_j + P_n(\lambda) + O(\lambda) \quad (3)$$

where $\sigma'_j(\lambda)$ is the differential absorption cross section of species j after removal of its broadband component, $P_n(\lambda)$ is an nth-order polynomial representing broadband extinction structures, and $O(\lambda)$ is an intensity-offset term. The SCD is defined as

$$\mathrm{SCD}_j = \int_L n_j(s)\, ds \quad (4)$$

https://doi.org/10.5194/egusphere-2026-4334
Preprint. Discussion started: 18 August 2026

where $n_j(s)$ is the number density of species j at position s along the effective light path L. In 2D MAX-DOAS measurements, the zenith spectrum recorded at 90° elevation within the same scan is commonly used as the Fraunhofer reference spectrum to minimize the effects of solar Fraunhofer structures, temporal variations in instrumental response, and stratospheric background absorption. For an elevation angle α, the differential slant column density (dSCD) is defined as

$$\mathrm{dSCD}_j(\alpha) = \mathrm{SCD}_j(\alpha) - \mathrm{SCD}_j(90°) \quad (5)$$

Because low-elevation 2D MAX-DOAS observations sample longer effective light paths through the lower boundary layer, the SCD difference between low-elevation and zenith observations primarily reflects tropospheric absorption. The dSCDs measured at multiple elevation angles can therefore be combined with air mass factors or weighting functions calculated using a radiative transfer model to retrieve tropospheric vertical column densities (VCDs) and vertical concentration profiles of trace gases.

Spectral fitting was performed using QDOAS version 3.6.5 (Fayt et al., 2024), with the zenith spectrum from each scan sequence serving as the Fraunhofer reference. The fitting settings are summarized in Table 2. The SAO2010 solar spectrum was used for wavelength calibration (Chance and Kurucz, 2010). Absorption cross sections for NO_2, HONO, HCHO, O_3, O_4, BrO, and H_2O were adopted from Vandaele et al. (1998), Stutz et al. (2000), Meller and Moortgat (2000), Serdyuchenko et al. (2014), Finkenzeller and Volkamer (2022), Fleischmann et al. (2004), and Polyansky et al. (2018), respectively. O_4 dSCDs measured at multiple elevation angles were first used to retrieve aerosol extinction profiles and constrain the effective light paths. The retrieved aerosol profiles were subsequently used as input for the trace-gas profile retrievals.

Table 2. DOAS spectral fitting settings for the NO_2/O_4 and HONO retrieval windows. A check mark (✓) indicates inclusion in the spectral fit, whereas an em dash (—) indicates exclusion.

Parameter	Data source or setting	NO_2/O_4	HONO
Fitting window (nm)	Spectral range	338–370	335–373
Reference spectrum	Mean of the zenith spectra recorded immediately before and after each elevation scan	✓	✓
Wavelength calibration	SAO2010 solar reference spectrum (Chance and Kurucz, 2010); spectral shift and stretch relative to the high-resolution solar atlas	✓	✓
NO_2	220 and 294 K; I_0 correction / orthogonalization (Vandaele et al., 1998)	✓	✓
HONO	296 K (Stutz et al., 2000)	—	✓
HCHO	298 K (Meller and Moortgat, 2000)	✓	✓
O_3	223 and 243 K; I_0 correction / orthogonalization (Serdyuchenko et al., 2014)	✓	✓
O_4	293 K (Finkenzeller and Volkamer, 2022)	✓	✓
BrO	223 K (Fleischmann et al., 2004)	✓	✓
H_2O	296 K (Polyansky et al., 2018)	—	✓
Ring spectra	Ring 1 and Ring 2	✓	✓
Polynomial order	5	✓	✓
Intensity offset		Slope / order 1	Constant + slope / order 1

https://doi.org/10.5194/egusphere-2026-4334
Preprint. Discussion started: 18 August 2026

2.2.3 Vertical profile retrievals with PriAM

Vertical profiles of aerosol extinction and trace-gas concentrations were retrieved using the profile inversion algorithm of aerosol extinction and trace gas concentration (PriAM). PriAM is an optimal-estimation-based algorithm developed by the Anhui Institute of Optics and Fine Mechanics, Chinese Academy of Sciences (AIOFM-CAS), in cooperation with the Max Planck Institute for Chemistry (MPIC), and has been evaluated in 2D MAX-DOAS profile-retrieval intercomparisons (Wang et al., 2013; Frieß et al., 2016, 2019). The nonlinear inverse problem is solved by iteratively adjusting aerosol extinction and trace-gas volume mixing ratio profiles under measurement-error and a priori constraints using a Levenberg–Marquardt-modified Gauss–Newton scheme (Rodgers, 2000; Frieß et al., 2019). SCIATRAN was used as the forward radiative transfer model to calculate weighting functions and simulated dSCDs (Rozanov et al., 2014; Frieß et al., 2019). The retrieval followed a two-step procedure: aerosol extinction profiles were first retrieved from O_4 dSCDs, and the resulting aerosol profiles were subsequently used to calculate trace-gas weighting functions and retrieve HONO and NO_2 profiles (Frieß et al., 2019; Tian et al., 2021).

$$J(\boldsymbol{x}) = [\boldsymbol{y} - \boldsymbol{F}(\boldsymbol{x})]^{\mathrm{T}} \boldsymbol{S}_{\mathbf{e}}^{-1} [\boldsymbol{y} - \boldsymbol{F}(\boldsymbol{x})] + [\boldsymbol{x} - \boldsymbol{x}_{\mathbf{a}}]^{\mathrm{T}} \boldsymbol{S}_{\mathrm{a}}^{-1} [\boldsymbol{x} - \boldsymbol{x}_{\mathbf{a}}] \quad (6)$$

In the cost function, $\boldsymbol{y}$ denotes the vector of measured dSCDs at different elevation angles, $\boldsymbol{x}$ is the retrieved state vector, $\boldsymbol{x}_{\mathbf{a}}$ is the a priori state vector, and $\boldsymbol{F(x)}$ is the corresponding forward-model simulation. The matrices $\boldsymbol{S}_{\mathbf{e}}$ and $\boldsymbol{S}_{\mathbf{a}}$ represent the measurement-error and a priori covariance matrices, respectively. Profiles were retrieved on a 21-level vertical grid spanning 0–4 km, with the lowest level at 0.05 km and the remaining levels spaced at 0.20 km intervals from 0.20 to 4.00 km.

2.2.4 Quality control and retrieval diagnostics

To comprehensively assess the quality and uncertainty of the 2D MAX-DOAS retrievals, quality control was applied at three stages: spectral fitting, profile retrieval, and statistical processing. Before field deployment, wavelength calibration was performed using a mercury lamp, followed by spectral alignment with a high-resolution solar reference spectrum. The spectrometers were temperature controlled to minimize wavelength drift and variations in dark current and instrumental line shape. Representative DOAS fits were evaluated by comparing measured and fitted spectra, fitting residuals, and the differential absorption features of HONO, NO_2, and O_4. Periods with hourly precipitation totals greater than 0 mm were excluded to reduce retrieval artefacts associated with rapid changes in effective light paths and reduced signal-to-noise ratios during precipitation. Near-surface air temperature, relative humidity, and precipitation were obtained from the ERA5 hourly single-level dataset (Copernicus Climate Change Service, 2018).

For the profile retrievals, the averaging kernel matrix (**A**) was used to characterize vertical sensitivity, while the degrees of freedom for signal (DOFS) quantified the total independent information content. The *i*th row of **A** represents the sensitivity of the retrieved value in layer *i* to perturbations in the true profile across all altitude layers. The DOFS is given by the trace of **A**:

$$\mathrm{DOFS} = \mathrm{tr}(\mathbf{A}) \quad (7)$$

https://doi.org/10.5194/egusphere-2026-4334
Preprint. Discussion started: 18 August 2026

DOFS represents the number of independent pieces of vertical information provided by the measurements, while the peak altitude and vertical width of each averaging kernel indicate the sensitivity range and effective vertical resolution of the corresponding retrieval layer. The altitude range constrained by the measurements was further evaluated by comparing the retrieved and a priori profiles. Representative spectral fits, averaging kernels, DOFS values, and retrieved and a priori profiles are presented in Sect. 3.1.

Aerosol optical depth (AOD) was used as the primary screening variable because trace-gas profile retrievals rely on aerosol retrievals to constrain effective light paths; anomalous aerosol retrievals can therefore compromise subsequent trace-gas retrievals (Frieß et al., 2019; Tian et al., 2021). When AOD was missing, negative, or greater than 3, the light-path constraint was considered unreliable, and all associated trace-gas products were discarded. Cases with $2 < \mathrm{AOD} \leqslant 3$ were further evaluated using a monthly median absolute deviation test applied to $\log_{10}$-transformed values, together with within-day time-series spike checks. NO_2 and HONO products were then screened separately to remove missing or non-positive values, monthly outliers, and short-lived spikes. The AOD thresholds were selected empirically based on the site-specific data distribution, time-series continuity, and manual inspection of anomalous cases. The valid VCD timestamps retained after screening were subsequently used to select the corresponding profile products, ensuring temporal consistency between the column and profile analyses.

To improve the statistical robustness of multi-day mean HONO profiles and time–height contour plots, observations were grouped into the relevant time and height bins, and the number of valid samples (N) was calculated for each bin. Only bins with $N \geqslant 5$ were retained for averaging, whereas those with $N < 5$ were excluded from subsequent statistical analyses and plotting because of insufficient representativeness. Limited interpolation and smoothing were applied only within the valid observational domain, with interpolation restricted to gaps bounded by valid observations. These procedures were used solely to improve the stability and readability of the mean profiles and contour plots and did not alter the quality-controlled observations used in the fertilization-event analysis or other quantitative calculations. The complete quality-control workflow, from raw-spectrum screening and spectral fitting to profile-product matching and statistical processing, is summarized in Fig. S1.

2.3 HONO photolysis frequency and OH production potential

To assess the potential contribution of HONO photolysis to boundary-layer oxidation, version 5.3.1 of the Tropospheric Ultraviolet and Visible (TUV) radiative transfer model was used to calculate the HONO photolysis frequency (Madronich and Flocke, 1999), J(HONO), at hourly resolution. The model inputs and parameter settings are summarized in Table S1 and include ERA5 total column ozone (TCO) and cloud variables (Copernicus Climate Change Service, 2018; Hersbach et al., 2020), NO_2 VCD and AOD retrieved from the 2D MAX-DOAS observations, prescribed aerosol optical properties, and the vertical and temporal grids. The NO_2 VCD was converted to Dobson units (DU) and supplied to TUV as the no2col input

https://doi.org/10.5194/egusphere-2026-4334
Preprint. Discussion started: 18 August 2026

parameter using 1 DU = 2.687 × 10^{16} molecules cm^{-2}. The AOD retrieved from 2D MAX-DOAS measurements at 360 nm was converted to its corresponding value at 550 nm, as required by TUV, using the Ångström power law (Ångström, 1964):

$$\mathrm{AOD}_{(550)} = \mathrm{AOD}_{(360)}(360/550)^{\theta} \quad (8)$$

where θ is the Ångström exponent. Because simultaneous multi-wavelength AOD observations were unavailable, baseline values of θ = 1.0 and single-scattering albedo (SSA) = 0.95 were prescribed. The sensitivity of the calculated J(HONO) to these aerosol optical assumptions was evaluated using a clear-sky case (5 March 2023, 12:00 UTC+8; τ_{cld} = 0) and a cloudy case (23 March 2023, 12:00 UTC+8; τ_{cld} = 101.41). Relative to the baseline values, θ was varied among 0.8, 1.2, and 1.5, whereas SSA was varied between 0.90 and 0.98. The results are presented in Fig. S4 and discussed in Sect. 3.4.

Using the conventional definition of the Dobson unit at standard temperature and pressure (STP), ERA5 TCO, provided in units of kg m^{-2}, was converted to DU before being used as the TUV input parameter o3col:

$$1\ \mathrm{DU} = 2.1415 \times 10^{-5}\ \mathrm{kg\ m^{-2}}$$

Cloud-related variables, including total cloud cover (TCC), low, medium, and high cloud cover, total column cloud liquid water (TCLW), total column cloud ice water (TCIW), and cloud-base height (CBH), were obtained from ERA5 and used to derive the cloud optical depth (τ_{cld}) and cloud-layer geometry required by TUV, including cloud-top height (z_{top}) and cloud-base height (z_{base}). Clear-sky and cloudy cases were classified using ERA5 TCC: cases with TCC < 0.05 were treated as clear sky and assigned τ_{cld} = 0, whereas those with TCC ≥ 0.05 were classified as cloudy. For cloudy cases, τ_{cld} was estimated from TCLW and TCIW, while z_{base} and z_{top} were derived from CBH and the dominant cloud layer; the corresponding formulas are provided in Table S1.

J(HONO) and its percentage changes were evaluated at 0.05, 0.20, and 0.40–2.00 km, with a vertical interval of 0.20 km above 0.20 km. Hourly J(HONO) values were matched to the corresponding 2D MAX-DOAS HONO number-density profiles at coincident times and heights. The potential OH production rate from HONO photolysis, $P(\mathrm{OH})_{\mathrm{HONO}}$, was then calculated as

$$P(\mathrm{OH})_{\mathrm{HONO}} = J(\mathrm{HONO}) \times [\mathrm{HONO}] \quad (9)$$

where J(HONO) is the HONO photolysis frequency (s^{-1}), [HONO] is the HONO number density (molecules cm^{-3}), and $P(\mathrm{OH})_{\mathrm{HONO}}$ is the potential OH production rate from HONO photolysis (molecules cm^{-3} s^{-1}).

2.4 Backward trajectories and potential source contribution function analysis

Backward trajectories were calculated using the Hybrid Single-Particle Lagrangian Integrated Trajectory (HYSPLIT) model and analysed using the TrajStat module in MeteoInfo (Wang et al., 2009; Wang, 2014). Potential source contribution function (PSCF) analysis was applied to identify potential source regions associated with elevated HONO concentrations (Ashbaugh et al., 1985). The study domain was divided into grid cells. For each cell, the total number of trajectory endpoints (n_{ij}) and the number associated with elevated HONO (m_{ij}) were counted. A weighting factor (W_{ij}) was applied to reduce uncertainty in cells containing only a small number of endpoints:

https://doi.org/10.5194/egusphere-2026-4334
Preprint. Discussion started: 18 August 2026

$$\mathrm{PSCF}_{ij} = \frac{m_{ij}}{n_{ij}} W_{ij} \tag{10}$$

A high PSCF value indicates that air masses traversing a given grid cell were more frequently associated with elevated HONO concentrations at the observation site. However, PSCF does not quantify emission fluxes and, by itself, cannot distinguish local emissions from short-range transport. Potential source regions were therefore interpreted in conjunction with the HONO observations and compared across different trajectory arrival heights.

3 Results and discussion

3.1 Retrieval quality and consistency of collocated systems

3.1.1 DOAS spectral fitting quality

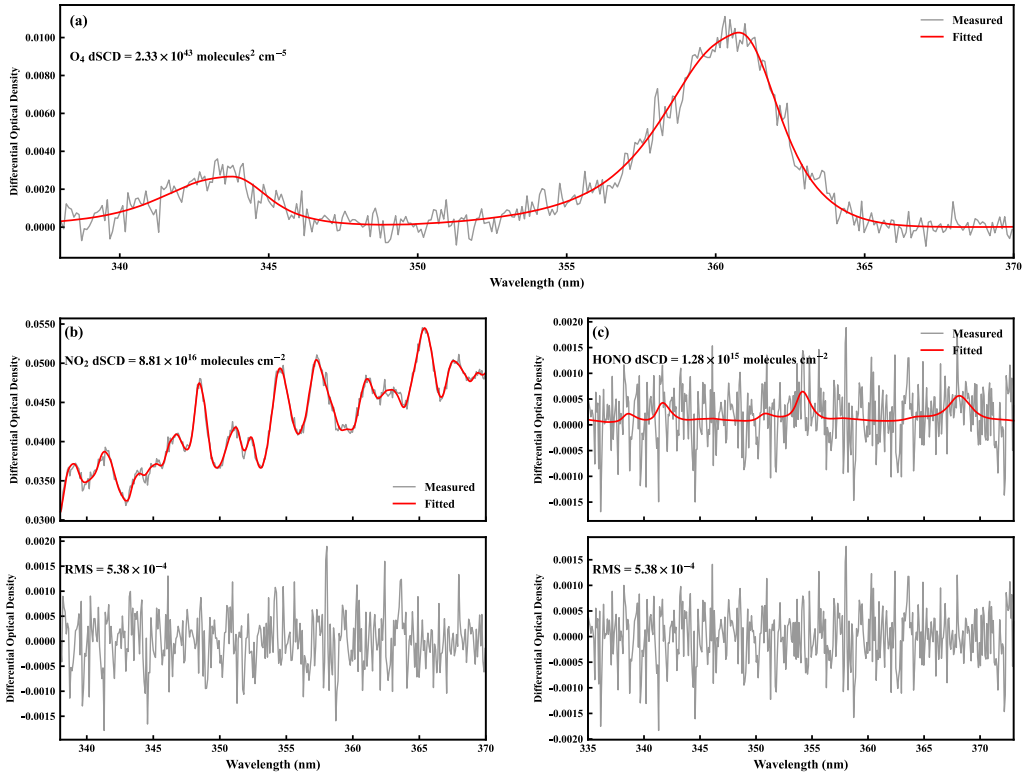

Figure 4. Representative DOAS spectral fits for O_4, NO_2, and HONO. Panels (a–c) show the fitted differential absorption structures and corresponding fit residuals for O_4, NO_2, and HONO, respectively. The spectra were recorded at 12:46:38 (UTC+8) on 14 December 2022, at an elevation angle of 8°, an azimuth angle of 18°, and a solar zenith angle of 56.42°.

Figure 4 presents representative DOAS fits for O_4, NO_2, and HONO obtained simultaneously under identical viewing geometry. The O_4 dSCD was 2.33 × 10^{43} molecules^2 cm^{-5}, and its characteristic absorption features near 344 and 360 nm were well

https://doi.org/10.5194/egusphere-2026-4334
Preprint. Discussion started: 18 August 2026

reproduced, providing a reliable constraint on the effective light path used in the aerosol profile retrieval. The NO_2 and HONO dSCDs were 8.81×10^{16} and 1.28×10^{15} molecules cm^{-2}, respectively, with root-mean-square (RMS) residuals of 5.38×10^{-4}. The NO_2 absorption features were distinct, and the measured and fitted spectra agreed closely. Although the HONO signal was weaker, its principal differential absorption features were still captured by the fitting model. The residuals for both species were randomly distributed around zero, with no discernible systematic structure. Overall, the adopted fitting settings adequately reproduced the major absorption features in the measured spectra and provided a reliable spectral basis for the subsequent aerosol and trace-gas profile retrievals.

3.1.2 Retrieval information content and vertical sensitivity

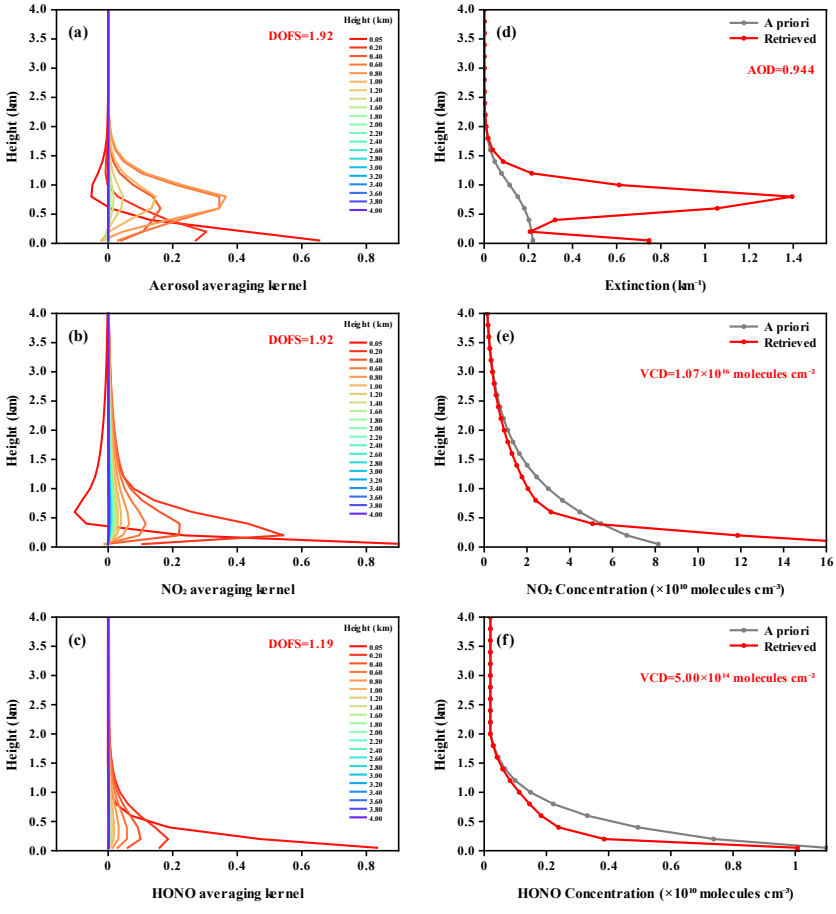

Figure 5. Representative PriAM profile retrievals and vertical sensitivities for aerosol extinction, NO_2, and HONO at 10:14:39 (UTC+8) on 3 June 2023. Panels (a–c) show the averaging kernels for aerosol extinction, NO_2, and HONO, respectively, with colours indicating the corresponding target layers at different heights. Panels (d–f) show the corresponding a priori profiles in grey and retrieved profiles in red.

https://doi.org/10.5194/egusphere-2026-4334
Preprint. Discussion started: 18 August 2026

Figure 5 demonstrates that the PriAM retrievals contain substantial measurement information in the lower atmosphere. The averaging kernels for aerosol extinction and NO_2 exhibited pronounced responses for target layers between 0.05 and 0.80 km. DOFS values of 1.92 for both retrievals indicate nearly two independent pieces of vertical information, reflecting sensitivity to both near-surface enhancements and elevated boundary-layer structures. The DOFS for HONO was 1.19, with the strongest sensitivity concentrated in the lowest layers, indicating meaningful measurement constraints on the near-surface HONO component despite its comparatively limited vertical information content. For all three products, the averaging-kernel responses weakened and broadened with increasing height, indicating that the retrievals were most strongly constrained near the surface and within the boundary layer. The retrieved aerosol extinction profile departed markedly from the a priori profile, revealing a near-surface enhancement and a distinct elevated layer at approximately 0.6–0.8 km, indicative of pronounced vertical stratification within the boundary layer. The retrieved NO_2 profile exhibited a strong near-surface maximum followed by a rapid decrease with height. The corresponding VCD was 1.07×10^{16} molecules cm^{-2}, and the profile shape indicated a pronounced near-surface contribution within the retrieved height range. HONO was likewise concentrated near the surface and declined sharply within the lowest 0.5 km, with a VCD of 5.00×10^{14} molecules cm^{-2}. This distribution is consistent with contributions from near-surface agricultural sources or surface production, together with the short atmospheric lifetime of HONO, which limits its upward transport. Taken together, the averaging-kernel patterns, DOFS values, and differences between the retrieved and a priori profiles support the reliability of the main retrieved lower-atmospheric features, particularly near the surface.

https://doi.org/10.5194/egusphere-2026-4334
Preprint. Discussion started: 18 August 2026

3.1.3 Consistency between the collocated systems

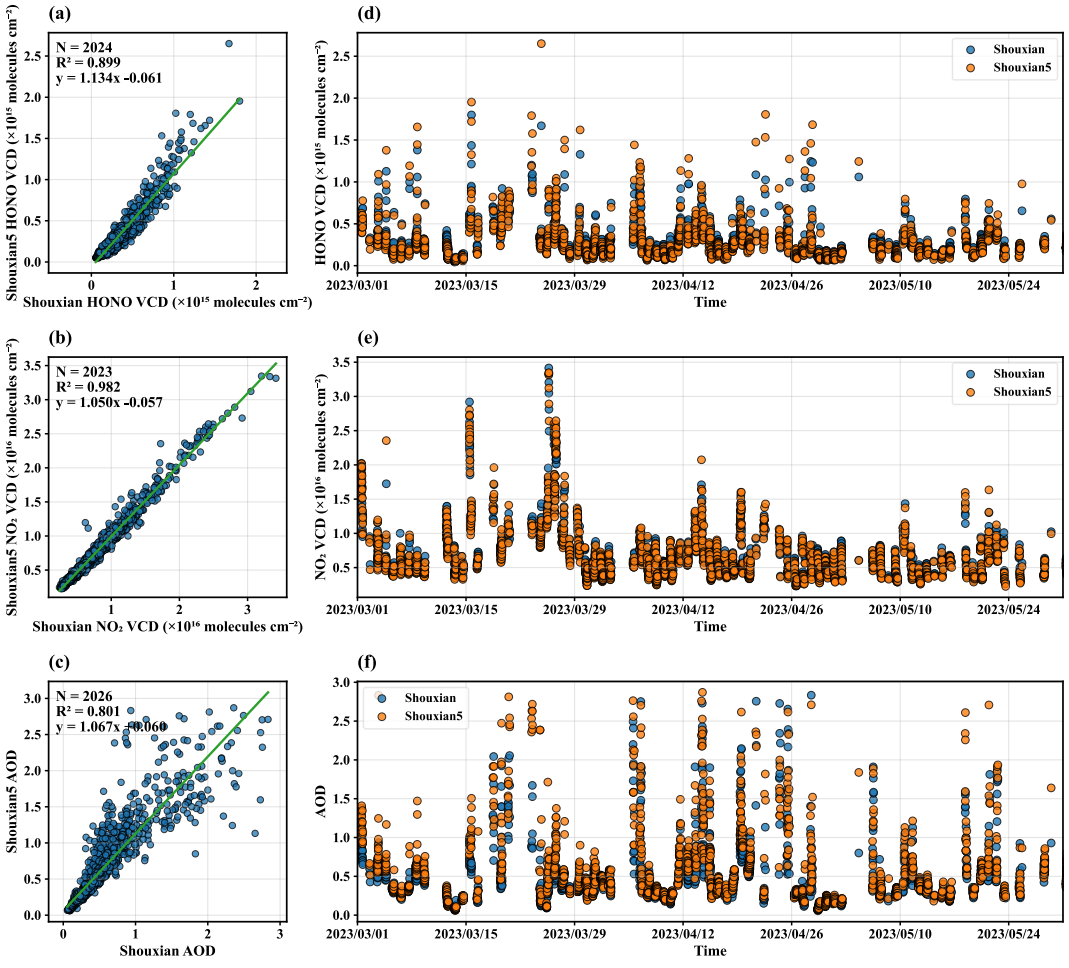

Figure 6. Intercomparison between the two collocated 2D MAX-DOAS systems at the Shouxian site. Panels (a–c) show scatter plots and linear regression results for HONO VCD, NO_2 VCD, and AOD, respectively, with the corresponding numbers of matched observations. Panels (d–f) show the corresponding time series from March to May 2023. The green lines indicate the linear regression fits.

Figure 6 compares temporally matched retrieval products from the two collocated 2D MAX-DOAS systems. The coefficients of determination (R^2) were 0.899 for HONO VCD, 0.982 for NO_2 VCD, and 0.801 for AOD, indicating that both systems consistently captured the dominant temporal variability in these products. The closest agreement was observed for NO_2, with the paired observations distributed near the 1:1 line and the corresponding time series exhibiting similar peaks and day-to-day variations. Despite its lower abundance and weaker differential absorption signal, HONO also showed good agreement between the two systems, which consistently captured the enhancement episodes during mid-to-late March and mid-April. AOD exhibited greater scatter, particularly at high values, potentially owing to aerosol spatial heterogeneity, cloud interference, and differences in retrieval sensitivity. Overall, the strong correlations and consistent temporal evolution demonstrate good

https://doi.org/10.5194/egusphere-2026-4334
Preprint. Discussion started: 18 August 2026

agreement between the two systems and support the consistency and stability of the retrieval products during the intercomparison period.

3.2 Spatiotemporal variability of HONO

This section examines the vertical distribution of HONO and its diurnal and seasonal variability in the Shouxian agricultural region based on the quality-controlled 2D MAX-DOAS retrievals.

3.2.1 Vertical distributions

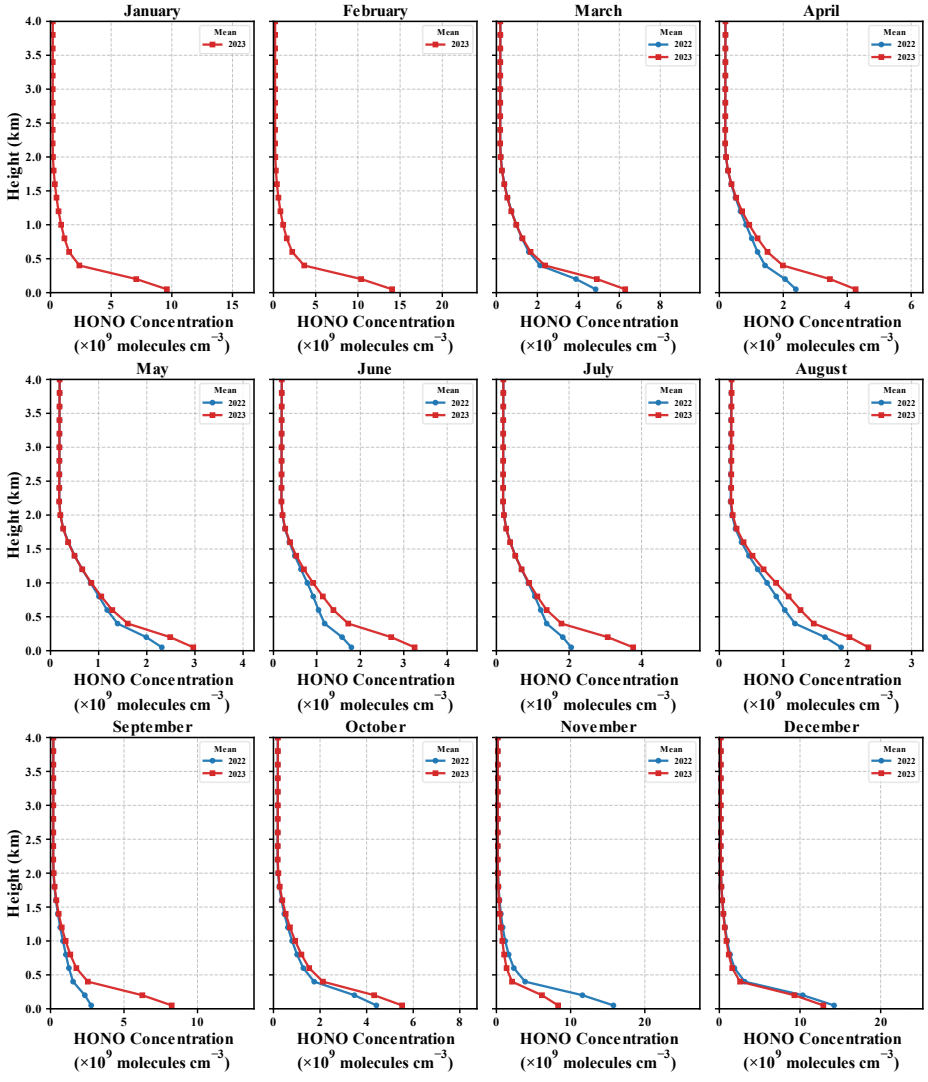

Figure 7. Monthly mean vertical profiles of HONO at Shouxian in 2022 and 2023. Blue and red lines represent the monthly mean profiles for 2022 and 2023, respectively. The horizontal axis shows HONO concentration, and the vertical axis shows height from 0 to 4 km.

https://doi.org/10.5194/egusphere-2026-4334
Preprint. Discussion started: 18 August 2026

The monthly mean profiles in Fig. 7 consistently show pronounced HONO enrichment near the surface, followed by a rapid decrease with height. The highest concentrations generally occurred within the lowest 0.2 km, declined substantially above 0.5 km, and remained relatively low above 1 km. This vertical pattern is consistent with previous surface-gradient and vertically resolved observations (VandenBoer et al., 2013; Wong et al., 2013; VandenBoer et al., 2014; Ryan et al., 2018) and suggests substantial contributions from soil and other surface-related processes, near-surface conversion of NO_2, and limited vertical redistribution. The short daytime lifetime of HONO may further limit the upward transport of near-surface enhancements into the upper boundary layer.

3.2.2 Daytime variation

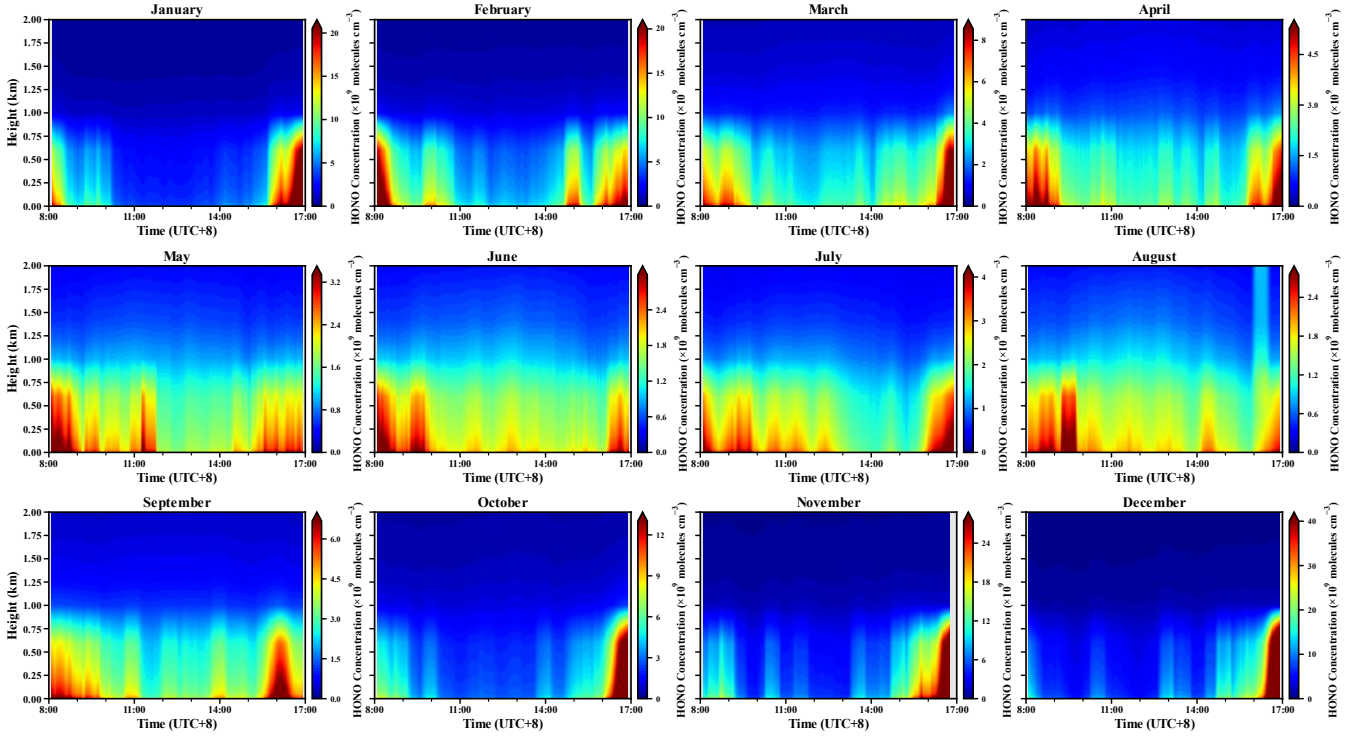

Figure 8. Two-year mean daytime height–time distributions of HONO at Shouxian for each calendar month during 2022–2023. Each panel shows the distribution averaged over the corresponding month in both years. The horizontal axis shows local time (UTC+8), the vertical axis shows height above ground level from 0 to 2 km, and the colour shading represents HONO concentration. Independent colour scales are used to highlight the daytime vertical structure within each month.

The monthly mean height–time distributions in Fig. 8 reveal pronounced daytime variations in HONO that differed with height and month. Near-surface HONO was generally enhanced in the morning and late afternoon, with lower concentrations around midday. At approximately 08:00, concentrations within the lowest 0.2 km frequently reached 5×10^9–2×10^{10} molecules cm^{-3}. These morning enhancements are consistent with the overnight accumulation of HONO within a shallow nocturnal boundary layer. From approximately 10:00 to 15:00, near-surface concentrations generally remained relatively low, at about 5×10^8–3

https://doi.org/10.5194/egusphere-2026-4334
Preprint. Discussion started: 18 August 2026

× 10^9 molecules cm^{-3}, consistent with enhanced photolytic loss and dilution as the boundary layer develops. However, the midday decrease was not vertically uniform. From April to August, relatively elevated HONO remained evident at approximately 0.4–1.0 km around midday, while concentrations in the lowest layers were comparatively lower. A similar but less pronounced elevated-layer feature was also observed in March and September. This height-dependent contrast may reflect the combined effects of boundary-layer evolution, vertical redistribution, and possible daytime HONO formation in elevated layers. After approximately 16:00, near-surface HONO increased again, with the most pronounced late-afternoon enhancements occurring in January, February, October, November, and December. Near-surface concentrations exceeded 1 × 10^{10} molecules cm^{-3} in several months and approached 4 × 10^{10} molecules cm^{-3} in December. The late-afternoon increase is consistent with weakening photolysis and renewed accumulation as the boundary layer becomes shallower (Wong et al., 2011; Li et al., 2012; Liu et al., 2019; Ye et al., 2023). The height-dependent daytime behaviour of HONO and its relationships with NO_2 and aerosol are examined further in Sect. 3.3.2 and Fig. 13.

3.2.3 Seasonal variation

For the seasonal analysis, meteorological seasons were defined as spring (March–May), summer (June–August), autumn (September–November), and winter (December–February), following the conventional seasonal classification for the Huai River Basin.

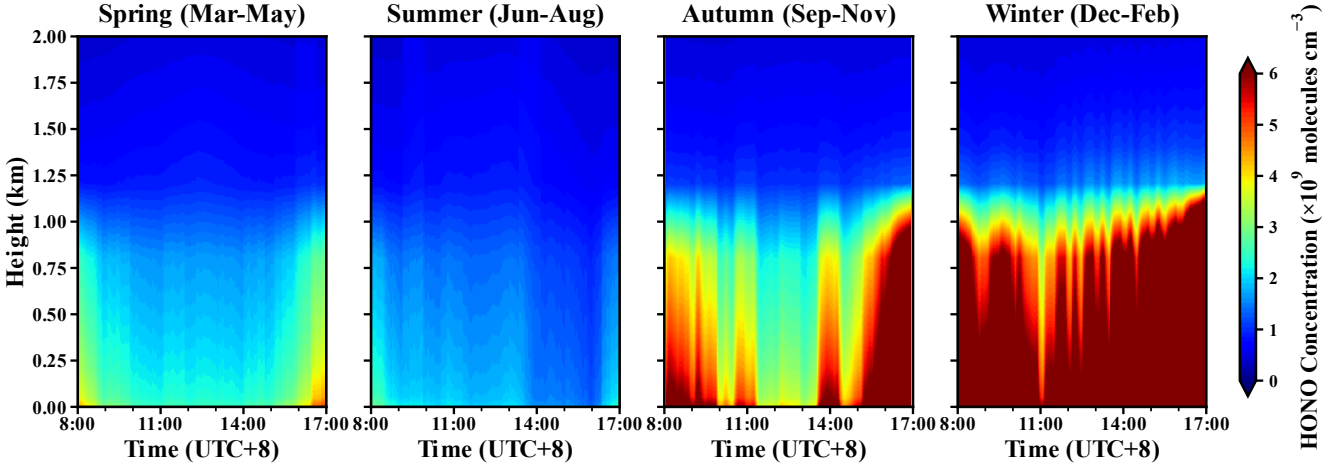

Figure 9. Two-year mean seasonal daytime height–time distributions of HONO at Shouxian based on observations from 2022–2023. The four panels show the distributions for spring, summer, autumn, and winter, respectively, with each seasonal distribution averaged over the corresponding seasons in both years. The horizontal axis shows local time (UTC+8), the vertical axis shows height from 0 to 2 km, and the colour shading represents HONO concentration.

All seasons in Fig. 9 show pronounced near-surface HONO enrichment. In autumn and winter, elevated HONO concentrations extended to approximately 0.8–1.0 km, a pattern consistent with weaker solar radiation, shallower boundary layers, and less efficient vertical dispersion. By contrast, summer HONO concentrations were generally lower and more strongly confined to the near-surface layer, likely owing to faster photolytic loss and more vigorous boundary-layer mixing. Spring showed

https://doi.org/10.5194/egusphere-2026-4334
Preprint. Discussion started: 18 August 2026

intermediate overall concentrations, which likely reflect the combined influences of agricultural activity, meteorological conditions, photochemistry, and boundary-layer development. In spring and summer, the midday decrease appeared to be less pronounced in elevated layers than near the surface, suggesting some height dependence in the daytime evolution of HONO. This feature is examined further in Sect. 3.3.2.

3.3 Potential controls and observational evidence

3.3.1 Meteorological and boundary-layer conditions

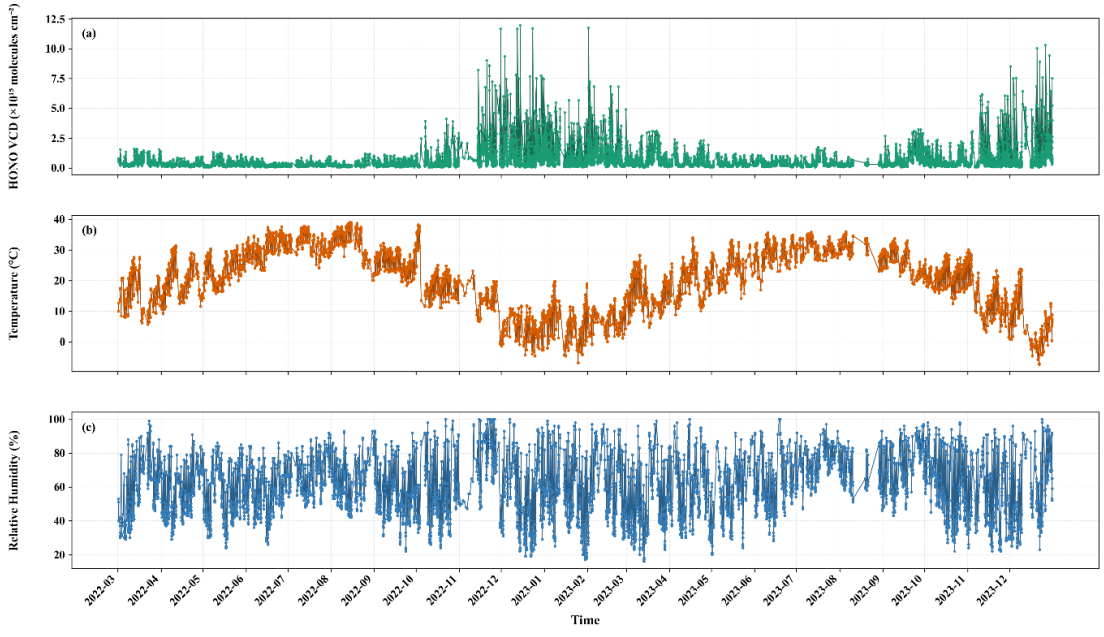

Figure 10. Time series of HONO VCD and near-surface meteorological variables at Shouxian during 2022–2023 (UTC+8). Panels (a–c) show HONO VCD, temperature, and relative humidity, respectively.

Figure 10 compares HONO VCD with simultaneous near-surface air temperature and relative humidity. Elevated HONO VCD frequently coincided with lower temperatures and higher relative humidity, particularly when relative humidity was approximately 70 %–90 %, suggesting meteorological conditions favourable for HONO accumulation. Lower temperatures are often associated with weaker solar radiation, slower HONO photolysis, and a shallower boundary layer, all of which can promote near-surface accumulation. Higher relative humidity can enhance the formation of surface water films on soil, vegetation, and aerosol particles, potentially facilitating heterogeneous NO_2 conversion. Conversely, during warmer periods with stronger solar radiation and a well-developed boundary layer, HONO can be removed more efficiently by photolysis and diluted through turbulent mixing. Because temperature, humidity, radiation, boundary-layer development, and optical-path conditions covary strongly, the observed co-occurrence highlights their combined influence on HONO variability.

https://doi.org/10.5194/egusphere-2026-4334
Preprint. Discussion started: 18 August 2026

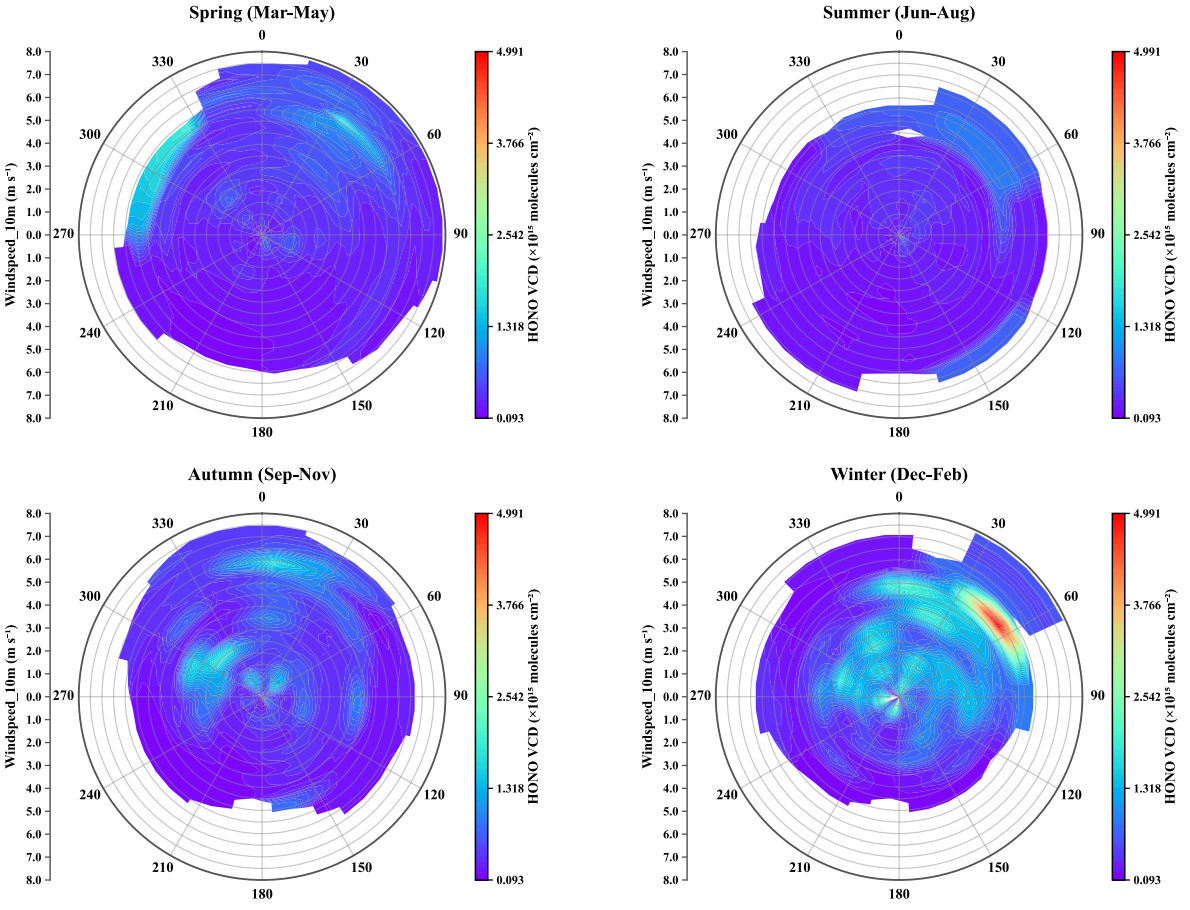

Figure 11. Two-year mean seasonal pollution roses showing HONO VCD as a function of wind direction and wind speed at Shouxian during 2022–2023. Panels (a–d) show spring, summer, autumn, and winter, respectively. The angular position indicates the upwind direction, the radial distance represents the 10 m wind speed, and the colour shading denotes HONO VCD.

Figure 11 further shows the seasonal dependence of HONO VCD on wind direction and wind speed. Elevated HONO VCD occurred more frequently under low-wind-speed conditions, consistent with near-surface accumulation under weak dispersion. The influence of wind direction was most evident in winter, when higher HONO VCD values were observed under northeasterly to east-northeasterly winds (approximately 30–70°) at wind speeds of 3–5 m s^{-1}. This pattern suggests that air masses arriving from this sector contributed to some wintertime HONO enhancement events. By contrast, the directional dependence was relatively weak in spring, summer, and autumn, indicating a smaller influence of air-mass origin during these seasons. Overall, the results suggest that wind direction exerted a stronger influence on HONO variability in winter, whereas local emissions and boundary-layer accumulation may have played more important roles in the other seasons. These potential influences are further examined using farming records and backward-trajectory analysis in Sect. 3.3.3.

https://doi.org/10.5194/egusphere-2026-4334
Preprint. Discussion started: 18 August 2026

3.3.2 Covariation with NO_2 and aerosol

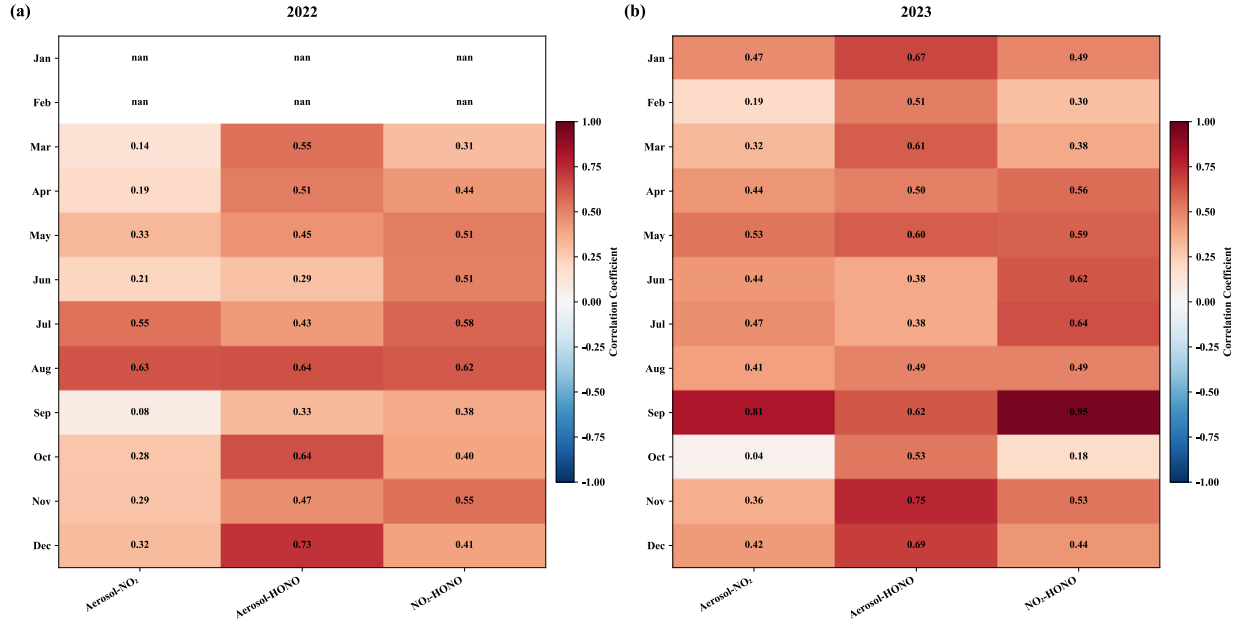

Figure 12. Monthly Pearson correlation coefficients among AOD, NO_2 VCD, and HONO VCD at Shouxian in (a) 2022 and (b) 2023. Each cell shows the corresponding correlation coefficient.

Figure 12 shows the monthly Pearson correlation coefficients among AOD, NO_2 VCD, and HONO VCD. Positive AOD–HONO and NO_2–HONO correlations occurred in most months, indicating that these variables covaried during much of the observation period. The AOD–HONO correlation coefficients generally ranged from 0.29 to 0.73 in 2022 and from 0.38 to 0.75 in 2023. The NO_2–HONO correlations exhibited greater month-to-month variability and reached a maximum of 0.95 in September 2023. The predominantly positive NO_2–HONO correlations are consistent with the role of NO_2 as a potential HONO precursor and with surface-related processes affecting both species, while the positive AOD–HONO correlations suggest possible links between HONO variability and aerosol-related surface chemistry or common accumulation conditions. Building on the correlations shown in Fig. 12, we further examined the two-year mean seasonal daytime evolution of the $HONO/NO_2$ ratio across different height layers (Fig. S2). The $HONO/NO_2$ ratio reflects the abundance of HONO relative to NO_2 and can serve as a qualitative indicator of HONO conversion and replenishment processes (Liu et al., 2019). Across all seasons, the ratio was generally highest at 0.05 km and decreased with height, consistent with preferential HONO formation or accumulation near the surface. In spring and summer, the ratio tended to increase from morning to midday across multiple height layers, with the clearest increase near the surface and progressively weaker changes aloft. The occurrence of this daytime increase across several layers suggests that radiation-associated HONO replenishment may have partly offset photolytic loss. To determine whether these ratio changes were driven primarily by HONO, NO_2, or both, Fig. 13 separately examines their height-resolved daytime variations.

https://doi.org/10.5194/egusphere-2026-4334
Preprint. Discussion started: 18 August 2026

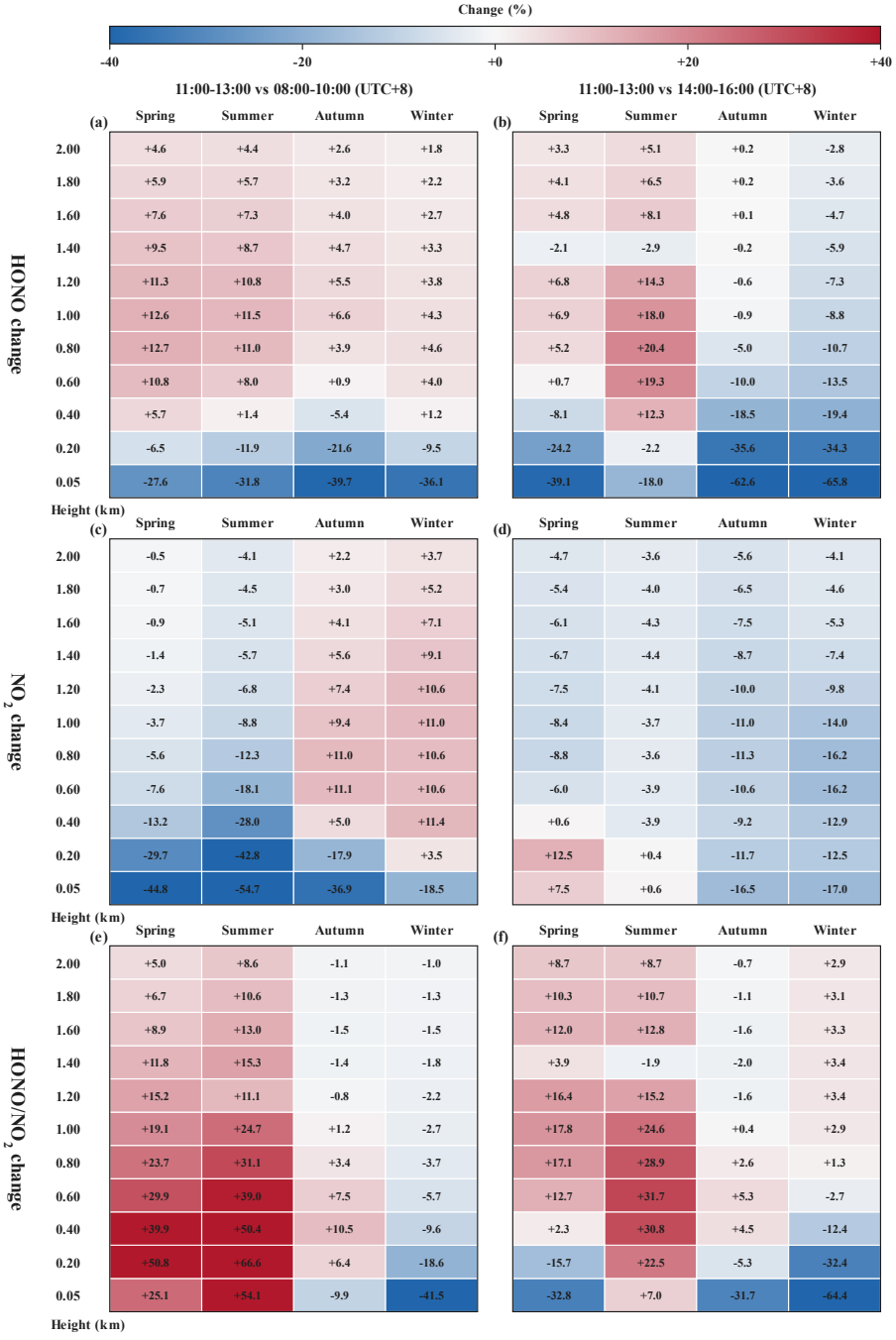

Figure 13. Two-year mean seasonal height-resolved relative changes in HONO, NO_2, and the HONO/NO_2 ratio at midday relative to the morning and afternoon at Shouxian during 2022–2023. Panels (a, c, e) show changes at 11:00–13:00 relative to 08:00–10:00, whereas panels (b, d, f) show changes at 11:00–13:00 relative to 14:00–16:00 (UTC+8). Panels (a, b), (c, d), and (e, f) correspond to HONO, NO_2, and HONO/NO_2, respectively. Positive and negative values indicate midday increases and decreases, respectively.

https://doi.org/10.5194/egusphere-2026-4334
Preprint. Discussion started: 18 August 2026

From morning to midday, HONO decreased markedly in the lowest layer in all seasons, with reductions of 27.6 %–39.7 % at 0.05 km and smaller decreases at 0.20 km. Above 0.6 km, however, HONO increased in all seasons, with the clearest enhancements observed in spring and summer. Between 0.6 and 1.2 km, midday HONO increased by 10.8 %–12.7 % in spring and 8.0 %–11.5 % in summer relative to the morning. This vertical contrast indicates that the daytime evolution of HONO differed between the near-surface and elevated layers. Near the surface, photolytic loss and boundary-layer dilution were likely dominant, whereas the net increase aloft suggests that HONO replenishment may have partly offset photolytic removal in the elevated layers.

The concurrent changes in NO_2 provide further insight into the elevated-layer HONO enhancement. From morning to midday, NO_2 decreased throughout the retrieved profile in spring and summer, with the largest reductions occurring at 0.05 km, where they reached 44.8 % and 54.7 %, respectively. Between 0.6 and 1.2 km, HONO increased while NO_2 decreased by approximately 2 %–18 %, resulting in HONO/NO_2 increases of approximately 11 %–39 %. These opposing changes are consistent with a possible contribution from NO_2-related conversion to daytime HONO replenishment. At the same time, differences in photochemical loss, vertical mixing, and other HONO sources may also have contributed to the observed relationship.

The comparison between midday and afternoon provides additional support for this interpretation. In summer, midday HONO between 0.6 and 1.2 km was approximately 14 %–20 % higher than in the afternoon, whereas NO_2 was approximately 4 % lower. The corresponding HONO/NO_2 ratio increased by approximately 15 %–32 %. Spring showed a similar but weaker pattern, with HONO increases of approximately 1 %–7 % and positive HONO/NO_2 changes over the same height range. The concurrent increase in HONO, decrease in NO_2, and enhancement of HONO/NO_2 indicate that the elevated-layer signal cannot be explained solely by declining NO_2 and suggest that net HONO production or replenishment contributed to the observed midday enhancement.

In autumn and winter, HONO and NO_2 generally increased together from morning to midday in the elevated layers, while the HONO/NO_2 response was weaker and less vertically coherent. Midday HONO was also generally lower than in the afternoon, particularly in winter. These seasonal differences indicate that the spring–summer pattern is more consistent with radiation-associated HONO replenishment. Possible pathways include light-enhanced heterogeneous conversion of NO_2 on aerosol surfaces and the photolysis of particulate nitrate within elevated layers, as well as surface production followed by the vertical redistribution of HONO or its precursors (Zhou et al., 2003; Stemmler et al., 2006; Ye et al., 2017; Xing et al., 2023). Overall, the concurrent increase in HONO, decrease in NO_2, and enhancement of HONO/NO_2 in spring and summer support the possibility that NO_2-related conversion contributed to daytime HONO replenishment.

https://doi.org/10.5194/egusphere-2026-4334
Preprint. Discussion started: 18 August 2026

3.3.3 Agricultural influences and the spring fertilization event

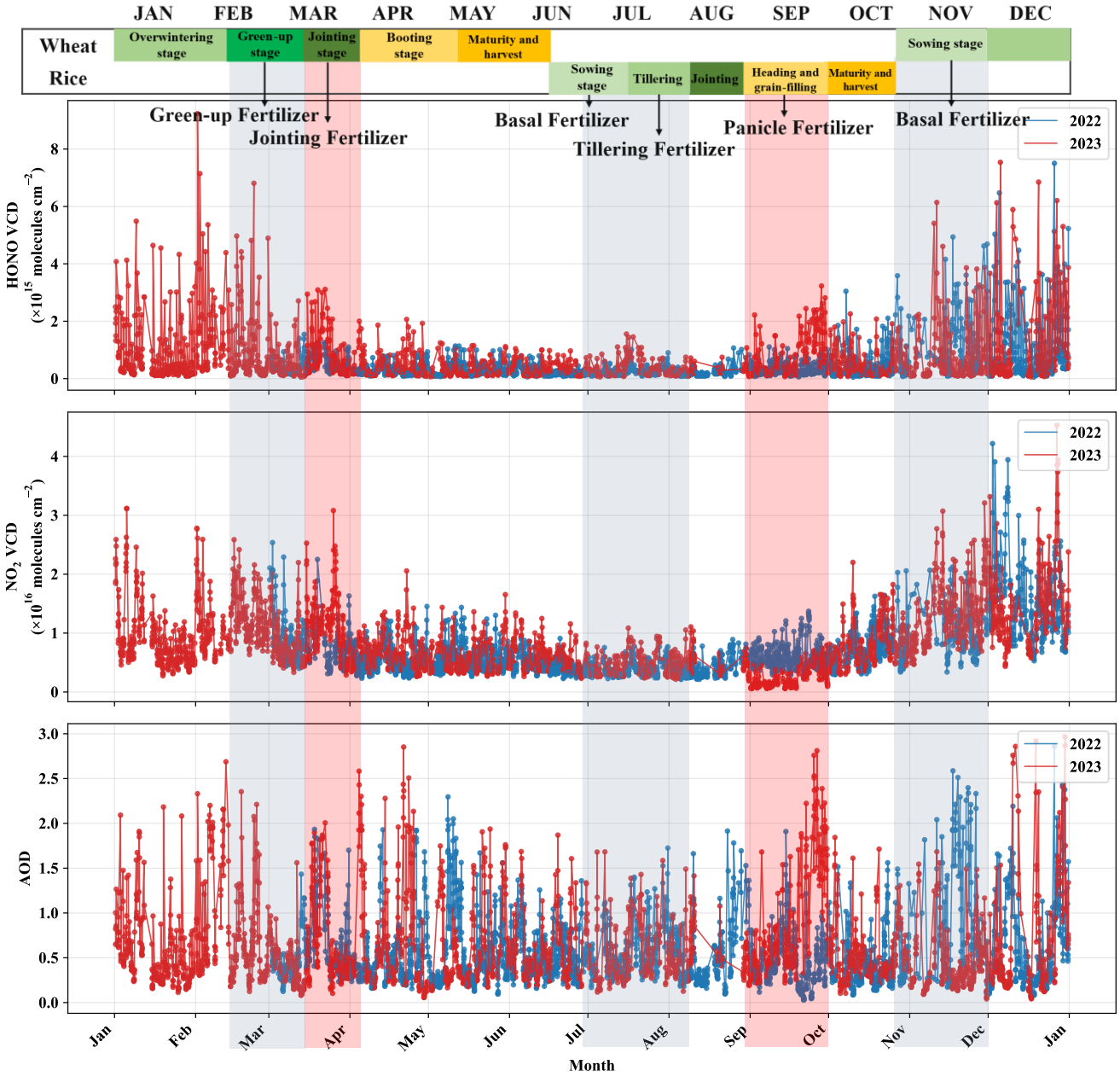

Figure 14. Temporal correspondence of HONO VCD, NO_2 VCD, and AOD with crop-growth stages and approximate fertilization windows at Shouxian during 2022–2023. The upper panel shows the wheat–rice rotation calendar and the main fertilization windows. The lower panels show the time series of HONO VCD, NO_2 VCD, and AOD, with blue and red representing 2022 and 2023, respectively.

https://doi.org/10.5194/egusphere-2026-4334
Preprint. Discussion started: 18 August 2026

Figure 14 shows that several HONO enhancement episodes occurred during periods of intensive agricultural activity, particularly around spring fertilization and pre-winter basal fertilization. This temporal correspondence is consistent with previous evidence that fertilization can enhance HONO emissions from agricultural soils (Wang et al., 2021; Song et al., 2023). During the approximate wheat green-up and jointing fertilization windows in March, HONO VCD repeatedly reached 2×10^{15}–5×10^{15} molecules cm^{-2}, with individual peaks approaching or exceeding 8×10^{15} molecules cm^{-2}. During the basal-fertilization window in November–December, HONO VCD peaks reached approximately 6×10^{15}–8×10^{15} molecules cm^{-2}. By contrast, HONO VCD was generally lower from May to August, mostly remaining below 1×10^{15} molecules cm^{-2}, although smaller episodic enhancements occurred around the approximate rice tillering-fertilization window in July–August.

NO_2 VCD increased concurrently with HONO during several periods and reached 2×10^{16}–4×10^{16} molecules cm^{-2} in winter and early spring, suggesting that changes in precursor abundance may have contributed to the observed HONO variability. AOD also increased during some periods of agricultural activity and field disturbance, occasionally reaching 1.5–3.0. The accompanying aerosol enhancement may have increased the available surfaces for heterogeneous HONO-related chemistry. Based on these temporal associations and previous field evidence, the documented fertilization event on 15 March 2023 was selected for further analysis.

https://doi.org/10.5194/egusphere-2026-4334
Preprint. Discussion started: 18 August 2026

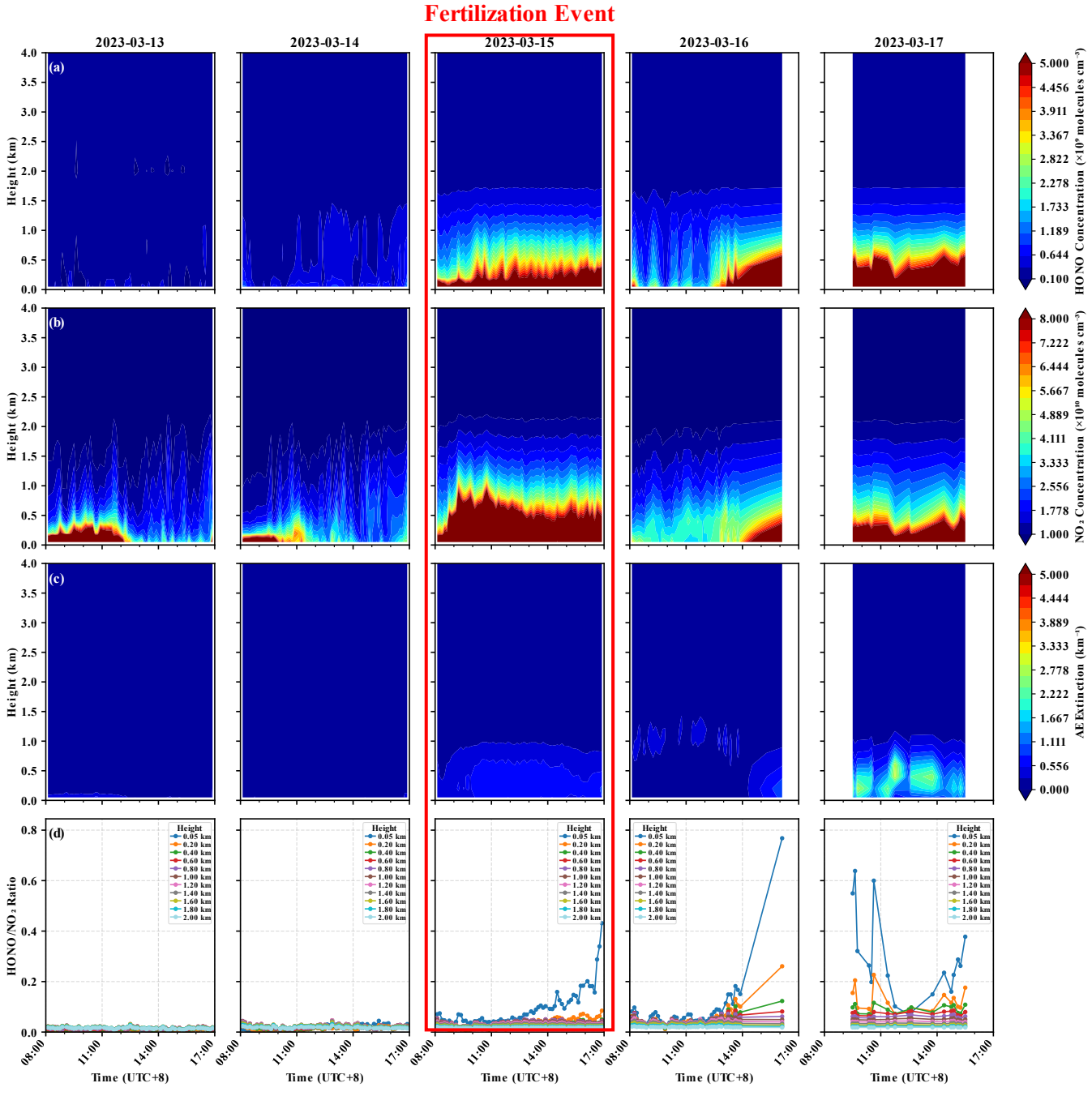

Figure 15. Height–time evolution of HONO, NO_2, and aerosol extinction during the fertilization event from 13 to 17 March 2023 (UTC+8). The red box highlights the recorded fertilization date of 15 March. Panels (a–c) show HONO concentration, NO_2 concentration, and aerosol extinction, respectively, while panel (d) shows the HONO/NO_2 ratio at height layers from 0.05 to 2.00 km.

Figure 15 shows the vertical evolution of HONO, NO_2, aerosol extinction, and the HONO/NO_2 ratio around the recorded fertilization event on 15 March 2023. HONO concentrations were relatively low during 13–14 March, with a mean of 4.92 ×

https://doi.org/10.5194/egusphere-2026-4334
Preprint. Discussion started: 18 August 2026

10^8 molecules cm^{-3} and a maximum of 3.87×10^9 molecules cm^{-3} at 0.05 km. On 15 March, HONO increased sharply, and the enhanced layer extended from the near surface to approximately 1.0–1.5 km. At 0.05 km, the mean concentration reached 1.38×10^{10} molecules cm^{-3}, approximately 28 times the pre-event mean, while the maximum reached 1.24×10^{11} molecules cm^{-3}, approximately 32 times the pre-event maximum. Elevated HONO persisted during 16–17 March, when the mean remained approximately 41 times the pre-event value. NO_2 also increased after fertilization, reaching approximately 6×10^{10}–8×10^{10} molecules cm^{-3} in the lowest layer, while aerosol extinction increased mainly below 1 km. The concurrent near-surface enhancement of HONO/NO_2 indicates that HONO increased more strongly than NO_2, supporting enhanced HONO formation or emission associated with soil- and surface-related processes after fertilization. Overall, the coordinated changes in HONO, NO_2, aerosol extinction, and HONO/NO_2 reveal a pronounced and sustained lower-boundary-layer response to the fertilization event.

Because the HONO enhancement persisted beyond the fertilization day, its robustness and sensitivity to the averaging-window length were further evaluated using post-to-pre-fertilization ratios calculated for equal-length windows of 1–14 d before and after 15 March 2023 (Fig. S3). The enhancement was evident across the different window lengths and remained concentrated mainly in the lower layers, indicating that the observed response was not dependent on a specific window choice. The 1–3 d windows were more sensitive to short-term peaks and limited sampling, whereas the 14 d window incorporated more of the subsequent recovery and lower-background periods. The 10 d window provided a suitable balance between capturing the sustained post-fertilization enhancement and reducing sensitivity to short-term variability and was therefore selected for the main pre- and post-fertilization comparison.

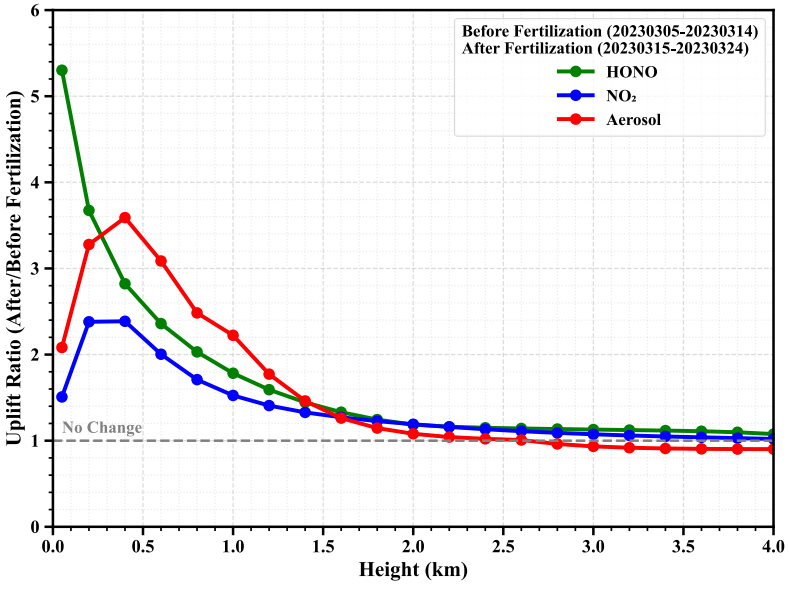

Figure 16. Post-to-pre-fertilization ratios of mean vertical profiles during the spring 2023 fertilization event. The pre- and post-fertilization periods each covered 10 d (5–14 and 15–24 March 2023, respectively). Green, blue, and red curves represent HONO, NO_2, and aerosol extinction, respectively; the grey dashed line at 1 indicates no change.

https://doi.org/10.5194/egusphere-2026-4334
Preprint. Discussion started: 18 August 2026

The 10 d mean profiles before and after fertilization showed distinct vertical responses (Fig. 16). The HONO post-to-pre-fertilization ratio reached 5.3 at 0.05 km, decreased to 3.7 at 0.20 km and approximately 2.5 at 0.50 km, and further declined to about 1.7 near 1.0 km and 1.1 above 2.0 km. This pattern indicates that the HONO enhancement was concentrated mainly below 1 km. By comparison, the NO_2 ratio showed a weaker response, peaking at approximately 2.3–2.4 between 0.2 and 0.4 km, while the aerosol-extinction ratio peaked at approximately 3.5–3.6 near 0.4 km. Thus, the vertical maxima of NO_2 and aerosol extinction occurred above that of HONO, and their enhancement factors near the surface were substantially smaller than that of HONO. This vertical mismatch indicates that the pronounced near-surface HONO increase was not simply proportional to either NO_2 accumulation or aerosol loading. Although the enhanced aerosol burden may have provided additional surfaces for heterogeneous reactions, it cannot alone explain the magnitude and near-surface maximum of the HONO response. Instead, the observations suggest a strong contribution from fertilization-induced soil emissions and surface production, together with boundary-layer mixing and vertical redistribution during the post-fertilization period.

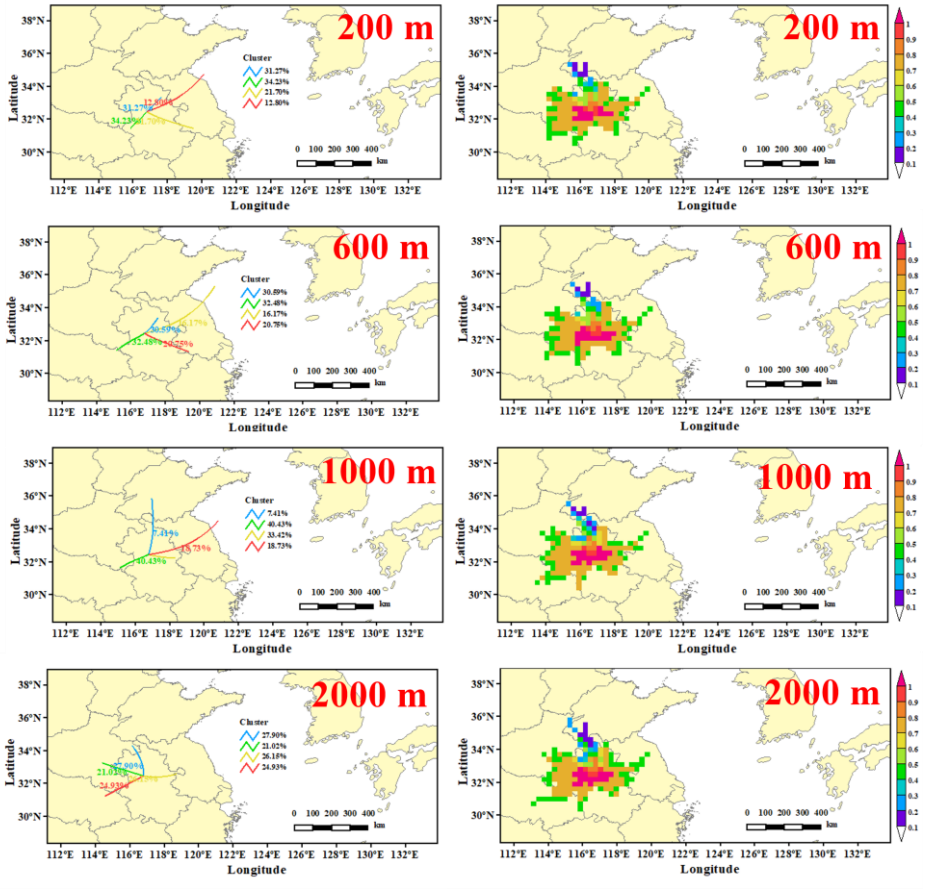

Figure 17. Clustered backward trajectories and potential HONO source regions for different arrival heights over Shouxian in March 2023. The left and right columns show the trajectory clusters and corresponding potential source contribution function (PSCF) distributions, respectively.

https://doi.org/10.5194/egusphere-2026-4334
Preprint. Discussion started: 18 August 2026

As discussed in Sect. 3.3.1, the directional dependence of HONO was relatively weak in spring, suggesting a smaller influence of air-mass origin during this season. The March backward trajectories and PSCF distributions in Fig. 17 provide further spatial information on the potential source regions. At all four arrival heights, the highest PSCF values were concentrated near Shouxian and the surrounding areas, with more localized near-site maxima at 200 and 600 m and broader spatial distributions at 1000 and 2000 m. As shown in Fig. 1, the observation site is surrounded predominantly by cultivated land, with no major industrial point sources identified nearby. The PSCF patterns therefore suggest substantial local and short-range agricultural influences, together with a possible contribution from broader regional transport at higher arrival heights. This interpretation is consistent with the pronounced near-surface HONO enhancement observed during the fertilization period. Overall, the agreement among the weak springtime directional dependence, surrounding agricultural land cover, near-site PSCF maxima, and vertical HONO response supports a substantial agricultural influence during the spring fertilization event.

3.4 Potential OH production from HONO photolysis

The sensitivity of TUV-derived J(HONO) to aerosol optical inputs was evaluated for representative clear-sky and cloudy cases in Fig. S4. Varying θ from 0.8 to 1.5 produced negligible changes in J(HONO) over 0.05–2.00 km in both cases, with differences close to zero at the plotting resolution. In contrast, sensitivity to SSA depended strongly on sky conditions. Under clear-sky conditions, changes in J(HONO) were limited to approximately −3 % to +2 %, whereas under cloudy conditions they ranged from approximately −30 % to +26 %, with the strongest response occurring in the lower layers. These results indicate that, among the two aerosol parameters tested, SSA represents the larger source of uncertainty for J(HONO) under the selected cloudy conditions. The baseline values of θ = 1.0 and SSA = 0.95 were therefore retained for the subsequent $P(\mathrm{OH})_{\mathrm{HONO}}$ calculations. This case-specific sensitivity test provides uncertainty context for the TUV results and highlights the increased importance of SSA under strong cloud attenuation.

Figure S5 shows the height-resolved distributions of J(HONO) averaged over the 10 d pre- and post-fertilization periods under clear-sky and cloudy conditions. Mean J(HONO) decreased after fertilization in the lower layers under both conditions. Under clear-sky conditions, the decrease weakened from approximately 15 % at 0.05 km to about 2 % at 2.00 km. Under cloudy conditions, the decrease was larger in the lower layers, reaching approximately 48 % at 0.05 km, but became progressively weaker with height and turned into an increase above approximately 1.4 km. These differences reflect variations in the radiation and cloud conditions sampled during the two 10 d periods, rather than changes in photolysis frequency directly associated with fertilization. Importantly, the lower-layer decrease in J(HONO) indicates that the post-fertilization increase in $P(\mathrm{OH})_{\mathrm{HONO}}$ was driven primarily by the substantial enhancement in HONO abundance rather than by stronger photolysis conditions.

https://doi.org/10.5194/egusphere-2026-4334
Preprint. Discussion started: 18 August 2026

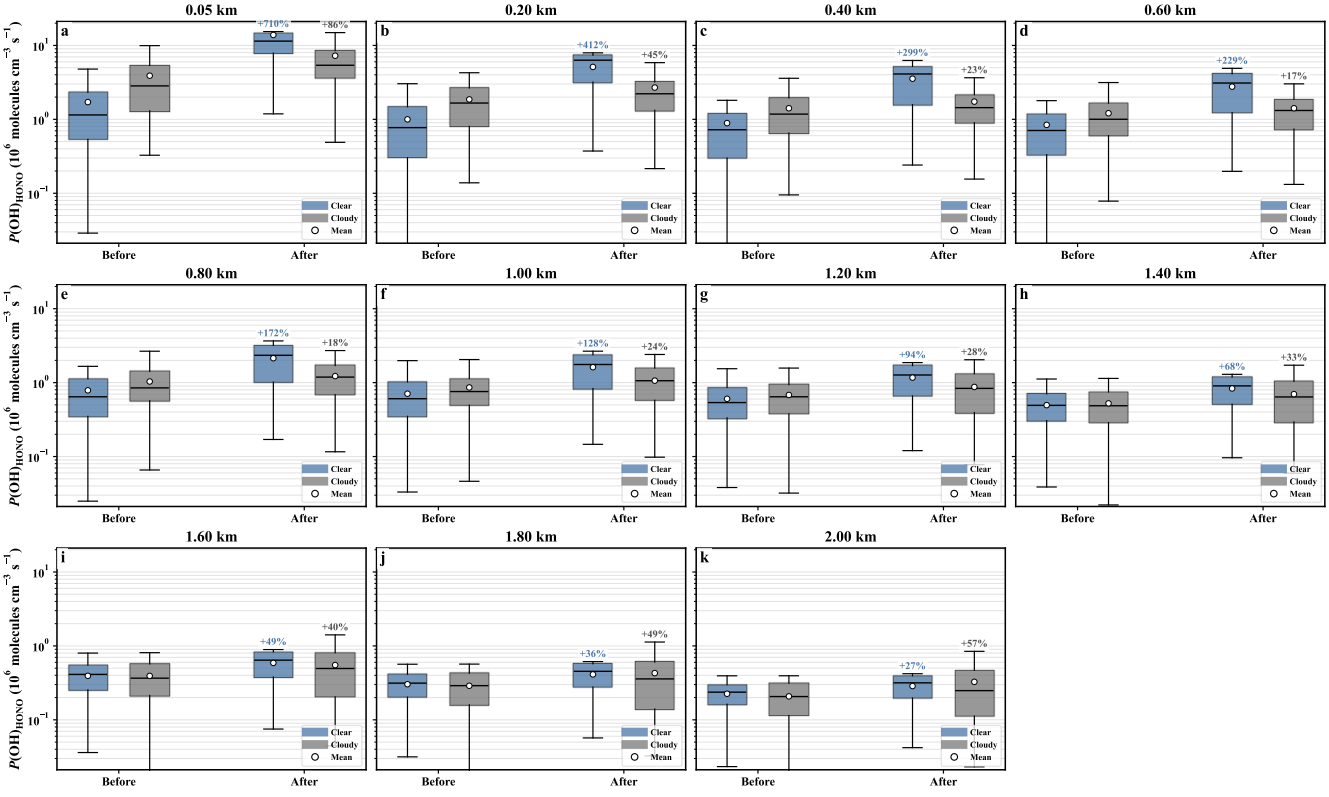

Figure 18. Vertical distributions of potential OH production from HONO photolysis under clear-sky and cloudy conditions before and after fertilization. The pre- and post-fertilization periods each covered 10 d (5–14 and 15–24 March 2023, respectively). Blue and grey boxes represent clear-sky and cloudy samples, respectively. Percentages indicate post-fertilization changes in the mean $P(OH)_{HONO}$ relative to the corresponding pre-fertilization mean.

Matching the 2D MAX-DOAS HONO concentration profiles with TUV-calculated J(HONO) yielded height-resolved estimates of $P(OH)_{HONO}$ (Fig. 18). To minimize the influence of differences in radiation conditions, the pre- and post-fertilization periods were compared separately under clear-sky and cloudy conditions. $P(OH)_{HONO}$ decreased rapidly with height, with the highest values occurring mainly between 0.05 and 0.40 km, consistent with the observed near-surface enrichment of HONO. Under clear-sky conditions, mean $P(OH)_{HONO}$ increased after fertilization by 710 %, 412 %, 299 %, and 229 % at 0.05, 0.20, 0.40, and 0.60 km, respectively. The enhancement weakened with height, decreasing from 172 % at 0.80 km to 68 % at 1.40 km and ranging from 27 % to 49 % between 1.60 and 2.00 km. This vertical gradient reflects the strongest HONO enhancement in the lowest layers and indicates a substantial post-fertilization increase in near-surface potential OH production.

Under cloudy conditions, the post-fertilization increase in $P(OH)_{HONO}$ ranged from 17 % to 86 % between 0.05 and 1.00 km. This enhancement was weaker than that under clear-sky conditions, indicating that reduced ultraviolet radiation partly offset the effect of the increased HONO abundance. At some heights, pre-fertilization $P(OH)_{HONO}$ under cloudy conditions exceeded the corresponding clear-sky values. This result likely reflects differences in HONO accumulation, boundary-layer structure,

https://doi.org/10.5194/egusphere-2026-4334
Preprint. Discussion started: 18 August 2026

and the meteorological conditions represented by the two sample groups, rather than a direct enhancement caused by cloud cover.

Overall, the post-fertilization period showed greater potential OH production from HONO photolysis, particularly under clear-sky conditions with stronger solar radiation. In the presence of sufficient co-reactants, this enhanced OH production potential could promote the oxidation of volatile organic compounds (VOCs) and other reduced species, thereby affecting ozone and secondary aerosol formation (Li et al., 2010; Li et al., 2011; Ye et al., 2023).

4 Conclusions and implications

Two years of 2D MAX-DOAS observations in the rice–wheat rotation region of Shouxian were used to retrieve vertical profiles of HONO, NO_2, and aerosol extinction. The measured and fitted spectra showed good agreement, and the characteristic absorption structures of the target species were reliably captured. The averaging kernels and degrees of freedom for signal (DOFS) further demonstrated that the retrieved profiles contained meaningful vertical information, with the strongest observational constraints in the lower boundary layer. The two collocated systems consistently captured the principal variations in HONO, NO_2, and aerosol optical depth (AOD), with R^2 values of 0.899, 0.982, and 0.801, respectively.

HONO was concentrated below 0.5 km and decreased rapidly with height. Daytime concentrations were generally higher in the morning and late afternoon than around midday, while seasonal mean concentrations followed the order winter > autumn > spring > summer. From morning to midday, HONO decreased in the lowest layers in all seasons but increased above approximately 0.6 km, with the clearest enhancements occurring in spring and summer. During these seasons, the increases in HONO aloft coincided with decreases in NO_2 and increases in the HONO/NO_2 ratio, and midday HONO also exceeded afternoon values at elevated heights, particularly in summer. This vertical contrast is consistent with radiation-associated daytime HONO replenishment in elevated layers and a possible contribution from NO_2-related conversion, although particulate nitrate photolysis, vertical transport, and other HONO sources may also have contributed. Elevated HONO frequently coincided with high relative humidity, weak winds, and meteorological conditions conducive to near-surface accumulation. Overall, HONO variability reflected the combined effects of photolysis, vertical mixing, surface chemistry, emissions, and meteorological conditions. Further observational and modelling constraints are required to quantify the relative contributions of these processes.

During the 10 d following the recorded fertilization event on 15 March 2023, mean HONO concentrations at 0.05, 0.20, and 0.50 km were 5.3, 3.7, and 2.5 times the corresponding values during the preceding 10 d, respectively, whereas changes above 2 km were small. NO_2 and aerosol extinction also changed during this period, but their vertical responses differed from that of HONO. Near-site PSCF maxima were evident at all arrival heights and were most localized at 200 and 600 m, suggesting stronger local and short-range influences. Collectively, these results indicate that the post-fertilization HONO enhancement was concentrated near the surface and was consistent with local and short-range agricultural influences. This interpretation agrees with previous field-flux evidence that agricultural nitrogen management can enhance HONO emissions. Further

https://doi.org/10.5194/egusphere-2026-4334
Preprint. Discussion started: 18 August 2026

measurements are required to quantify the relative contributions of soil nitrogen transformation, surface reactions, and short-range transport.

Potential OH production from HONO photolysis was higher after fertilization under both clear-sky and cloudy conditions. At 0.05 km, the mean $P(OH)_{HONO}$ increased by 710 % for clear-sky samples and 86 % for cloudy samples, and the percentage increase generally decreased with height. The TUV sensitivity tests showed little response of $J(HONO)$ to the tested θ range in the selected cases, but a stronger response to SSA under cloudy conditions. These results indicate that HONO photolysis provided an enhanced potential OH source after fertilization, especially near the surface and under stronger radiation. However, $P(OH)_{HONO}$ represents a potential production rate rather than a direct OH measurement; quantifying the contribution of HONO to total atmospheric oxidation, ozone production, and secondary-aerosol formation would require direct radical observations or chemical modelling.

Interpretation of the fertilization event was also limited by the lack of concurrent measurements of soil HONO fluxes, fertilizer-application rates, soil physicochemical and microbial properties, boundary-layer height, and OH/HO_2. Future studies integrating these measurements with multi-site, vertically resolved observations and regional chemical modelling would improve process attribution, better quantify agricultural HONO sources and transformations, and clarify their implications for atmospheric oxidation and air quality.

Data availability

The 2022–2023 2D MAX-DOAS observations at Shouxian will be made available through a public data repository. Near-surface air temperature, relative humidity, precipitation, total-column ozone, and cloud variables used in the TUV calculations were obtained from the ERA5 hourly single-level dataset, available at https://doi.org/10.24381/cds.adbb2d47 (Copernicus Climate Change Service, 2018).

Author contributions

WWH conceived the study, processed and analysed the data, interpreted the results, prepared the figures, and wrote the original draft. AL supervised the project, acquired funding, contributed to the study design and interpretation, and reviewed and edited the manuscript. MQ provided the farming activity and fertilization records for Shouxian and contributed to the interpretation of the results. ZKH contributed to the methodology, data analysis strategy, interpretation of the results, and manuscript review. HMR, HRZ, JMX, and CNL contributed to observational data curation, data analysis, and scientific discussion. All authors discussed the results and reviewed and approved the final manuscript.

https://doi.org/10.5194/egusphere-2026-4334
Preprint. Discussion started: 18 August 2026

Competing interests

The authors declare that they have no conflict of interest.

Acknowledgements

The authors gratefully acknowledge the Shouxian National Climate Observatory for providing the observation site, infrastructure, and field support. We thank the staff involved in the installation, operation, maintenance, and quality assurance of the 2D MAX-DOAS instruments. We acknowledge the Royal Belgian Institute for Space Aeronomy (BIRA-IASB) for providing QDOAS, the U.S. National Science Foundation National Center for Atmospheric Research (NSF NCAR) for maintaining the TUV model, and the Copernicus Climate Change Service and the European Centre for Medium-Range Weather Forecasts (ECMWF) for providing ERA5 data. We also acknowledge the National Oceanic and Atmospheric Administration Air Resources Laboratory (NOAA ARL) for developing and providing the HYSPLIT model and Yaqiang Wang for developing MeteoInfo and its TrajStat module used for the trajectory and PSCF analyses. We thank all colleagues who contributed to the observations, data analysis, discussions, and manuscript preparation.

Financial support

This research was supported by the National Key Research and Development Program of China (Grant Nos. 2022YFC3703500 and 2023YFC3705800).

References

Alicke, B., Geyer, A., Hofzumahaus, A., Holland, F., Konrad, S., Pätz, H.-W., Schäfer, J., Stutz, J., Volz-Thomas, A., and Platt, U.: OH formation by HONO photolysis during the BERLIOZ experiment, J. Geophys. Res.-Atmos., 108, 8247, https://doi.org/10.1029/2001JD000579, 2003.

Ångström, A.: The parameters of atmospheric turbidity, Tellus, 16, 64–75, https://doi.org/10.3402/tellusa.v16i1.8885, 1964.

Ashbaugh, L. L., Malm, W. C., and Sadeh, W. Z.: A residence time probability analysis of sulfur concentrations at Grand Canyon National Park, Atmos. Environ., 19, 1263–1270, https://doi.org/10.1016/0004-6981(85)90256-2, 1985.

Bhattarai, H. R., Wanek, W., Siljanen, H. M. P., Ronkainen, J. G., Liimatainen, M., Hu, Y., Nykänen, H., Biasi, C., and Maljanen, M.: Denitrification is the major nitrous acid production pathway in boreal agricultural soils, Commun. Earth Environ., 2, 54, https://doi.org/10.1038/s43247-021-00125-7, 2021.

Chen, J., Chen, J., Liao, A., Cao, X., Chen, L., Chen, X., He, C., Han, G., Peng, S., Lu, M., Zhang, W., Tong, X., and Mills, J.: Global land cover mapping at 30 m resolution: A POK-based operational approach, ISPRS J. Photogramm. Remote Sens., 103, 7–27, https://doi.org/10.1016/j.isprsjprs.2014.09.002, 2015.

https://doi.org/10.5194/egusphere-2026-4334
Preprint. Discussion started: 18 August 2026

Chance, K. and Kurucz, R. L.: An improved high-resolution solar reference spectrum for Earth's atmosphere measurements in the ultraviolet, visible, and near infrared, J. Quant. Spectrosc. Ra., 111, 1289–1295, https://doi.org/10.1016/j.jqsrt.2010.01.036, 2010.

Copernicus Climate Change Service (C3S): ERA5 hourly data on single levels from 1940 to present, Copernicus Climate Change Service Climate Data Store (CDS) [data set], https://doi.org/10.24381/cds.adbb2d47, 2018.

Fayt, C., Danckaert, T., Van Roozendael, M., and Vlietinck, J.: QDOAS trace gas retrieval software, Royal Belgian Institute for Space Aeronomy [code], https://doi.org/10.18758/oqvqk2j3, 2024.

Finkenzeller, H. and Volkamer, R.: O_2–O_2 collision-induced absorption in the gas phase: cross-section of weak bands and continuum absorption between 297 and 500 nm, J. Quant. Spectrosc. Ra., 279, 108063, https://doi.org/10.1016/j.jqsrt.2021.108063, 2022.

Fleischmann, O. C., Hartmann, M., Burrows, J. P., and Orphal, J.: New ultraviolet absorption cross-sections of BrO at atmospheric temperatures measured by time-windowing Fourier transform spectroscopy, J. Photoch. Photobio. A, 168, 117–132, https://doi.org/10.1016/j.jphotochem.2004.03.026, 2004.

Frieß, U., Beirle, S., Alvarado Bonilla, L., Bösch, T., Friedrich, M. M., Hendrick, F., Piters, A., Richter, A., van Roozendael, M., Rozanov, V. V., Spinei, E., Tirpitz, J.-L., Vlemmix, T., Wagner, T., and Wang, Y.: Intercomparison of MAX-DOAS vertical profile retrieval algorithms: studies using synthetic data, Atmos. Meas. Tech., 12, 2155–2181, https://doi.org/10.5194/amt-12-2155-2019, 2019.

Frieß, U., Klein Baltink, H., Beirle, S., Clémer, K., Hendrick, F., Henzing, B., Irie, H., de Leeuw, G., Li, A., Moerman, M. M., van Roozendael, M., Shaiganfar, R., Wagner, T., Wang, Y., Xie, P., Yilmaz, S., and Zieger, P.: Intercomparison of aerosol extinction profiles retrieved from MAX-DOAS measurements, Atmos. Meas. Tech., 9, 3205–3222, https://doi.org/10.5194/amt-9-3205-2016, 2016.

Frieß, U., Monks, P. S., Remedios, J. J., Rozanov, A., Sinreich, R., Wagner, T., and Platt, U.: MAX-DOAS O_4 measurements: a new technique to derive information on atmospheric aerosols – 2. Modeling studies, J. Geophys. Res.-Atmos., 111, D14203, https://doi.org/10.1029/2005JD006618, 2006.

Gan, C., Li, B., Dong, J., Li, Y., Zhao, Y., Wang, T., Yang, Y., and Liao, H.: Atmospheric HONO emissions in China: unraveling the spatiotemporal patterns and their key influencing factors, Environ. Pollut., 343, 123228, https://doi.org/10.1016/j.envpol.2023.123228, 2024.

Hersbach, H., Bell, B., Berrisford, P., Hirahara, S., Horányi, A., Muñoz-Sabater, J., Nicolas, J., Peubey, C., Radu, R., Schepers, D., Simmons, A., Soci, C., Abdalla, S., Abellan, X., Balsamo, G., Bechtold, P., Biavati, G., Bidlot, J., Bonavita, M., De Chiara, G., Dahlgren, P., Dee, D., Diamantakis, M., Dragani, R., Flemming, J., Forbes, R., Fuentes, M., Geer, A., Haimberger, L., Healy, S., Hogan, R. J., Hólm, E., Janisková, M., Keeley, S., Laloyaux, P., Lopez, P., Lupu, C., Radnoti, G., de Rosnay, P., Rozum, I., Vamborg, F., Villaume, S., and Thépaut, J.-N.: The ERA5 global reanalysis, Q. J. Roy. Meteor. Soc., 146, 1999–2049, https://doi.org/10.1002/qj.3803, 2020.

https://doi.org/10.5194/egusphere-2026-4334
Preprint. Discussion started: 18 August 2026

Hönninger, G., von Friedeburg, C., and Platt, U.: Multi axis differential optical absorption spectroscopy (MAX-DOAS), Atmos. Chem. Phys., 4, 231–254, https://doi.org/10.5194/acp-4-231-2004, 2004.

Kleffmann, J.: Daytime sources of nitrous acid (HONO) in the atmospheric boundary layer, ChemPhysChem, 8, 1137–1144, https://doi.org/10.1002/cphc.200700016, 2007.

Laufs, S., Cazaunau, M., Stella, P., Kurtenbach, R., Cellier, P., Mellouki, A., Loubet, B., and Kleffmann, J.: Diurnal fluxes of HONO above a crop rotation, Atmos. Chem. Phys., 17, 6907–6923, https://doi.org/10.5194/acp-17-6907-2017, 2017.

Li, G., Lei, W., Zavala, M., Volkamer, R., Dusanter, S., Stevens, P., and Molina, L. T.: Impacts of HONO sources on the photochemistry in Mexico City during the MCMA-2006/MILAGO Campaign, Atmos. Chem. Phys., 10, 6551–6567, https://doi.org/10.5194/acp-10-6551-2010, 2010.

Li, X., Brauers, T., Häseler, R., Bohn, B., Fuchs, H., Hofzumahaus, A., Holland, F., Lou, S., Lu, K. D., Rohrer, F., Hu, M., Zeng, L. M., Zhang, Y. H., Garland, R. M., Su, H., Nowak, A., Wiedensohler, A., Takegawa, N., Shao, M., and Wahner, A.: Exploring the atmospheric chemistry of nitrous acid (HONO) at a rural site in southern China, Atmos. Chem. Phys., 12, 1497–1513, https://doi.org/10.5194/acp-12-1497-2012, 2012.

Li, Y., An, J., Min, M., Zhang, W., Wang, F., and Xie, P.: Impacts of HONO sources on the air quality in Beijing, Tianjin and Hebei Province of China, Atmos. Environ., 45, 4735–4744, https://doi.org/10.1016/j.atmosenv.2011.04.086, 2011.

Liu, Y., Nie, W., Xu, Z., Wang, T., Wang, R., Li, Y., Wang, L., Chi, X., and Ding, A.: Semi-quantitative understanding of source contribution to nitrous acid (HONO) based on 1 year of continuous observation at the SORPES station in eastern China, Atmos. Chem. Phys., 19, 13289–13308, https://doi.org/10.5194/acp-19-13289-2019, 2019.

Madronich, S. and Flocke, S.: The role of solar radiation in atmospheric chemistry, in: Environmental Photochemistry, The Handbook of Environmental Chemistry, vol. 2L, edited by: Boule, P., Springer, Berlin and Heidelberg, 1–26, https://doi.org/10.1007/978-3-540-69044-3_1, 1999.

Meller, R. and Moortgat, G. K.: Temperature dependence of the absorption cross sections of formaldehyde between 223 and 323 K in the wavelength range 225–375 nm, J. Geophys. Res.-Atmos., 105, 7089–7101, https://doi.org/10.1029/1999JD901074, 2000.

Meng, F., Han, B., Qin, M., Fang, W., Tang, K., Shao, D., Liao, Z., Duan, J., Feng, Y., Huang, Y., Ni, T., and Xie, P.: Measurement report: surface exchange fluxes of HONO during the growth process of paddy fields in the Huaihe River Basin, China, Atmos. Chem. Phys., 24, 14191–14208, https://doi.org/10.5194/acp-24-14191-2024, 2024.

Meng, F., Qin, M., Fang, W., Duan, J., Tang, K., Zhang, H., Shao, D., Liao, Z., Feng, Y., Huang, Y., Ni, T., Xie, P., Liu, J., and Liu, W.: Measurement of HONO flux using the aerodynamic gradient method over an agricultural field in the Huaihe River Basin, China, J. Environ. Sci., 114, 297–307, https://doi.org/10.1016/j.jes.2021.09.005, 2022.

Oswald, R., Behrendt, T., Ermel, M., Wu, D., Su, H., Cheng, Y., Breuninger, C., Moravek, A., Mougin, E., Delon, C., Loubet, B., Pommerening-Röser, A., Sörgel, M., Pöschl, U., Hoffmann, T., Andreae, M. O., Meixner, F. X., and Trebs, I.: HONO emissions from soil bacteria as a major source of atmospheric reactive nitrogen, Science, 341, 1233–1235, https://doi.org/10.1126/science.1242266, 2013.

https://doi.org/10.5194/egusphere-2026-4334
Preprint. Discussion started: 18 August 2026

Platt, U. and Stutz, J.: Differential Optical Absorption Spectroscopy: Principles and Applications, Springer, Berlin and Heidelberg, https://doi.org/10.1007/978-3-540-75776-4, 2008.

Polyansky, O. L., Kyuberis, A. A., Zobov, N. F., Tennyson, J., Yurchenko, S. N., and Lodi, L.: ExoMol molecular line lists XXX: a complete high-accuracy line list for water, Mon. Not. R. Astron. Soc., 480, 2597–2608, https://doi.org/10.1093/mnras/sty1877, 2018.

Rodgers, C. D.: Inverse Methods for Atmospheric Sounding: Theory and Practice, World Scientific, Singapore, https://doi.org/10.1142/3171, 2000.

Rozanov, V. V., Rozanov, A. V., Kokhanovsky, A. A., and Burrows, J. P.: Radiative transfer through terrestrial atmosphere and ocean: software package SCIATRAN, J. Quant. Spectrosc. Ra., 133, 13–71, https://doi.org/10.1016/j.jqsrt.2013.07.004, 2014.

Ryan, R. G., Rhodes, S., Tully, M., Wilson, S., Jones, N., Frieß, U., and Schofield, R.: Daytime HONO, NO_2 and aerosol distributions from MAX-DOAS observations in Melbourne, Atmos. Chem. Phys., 18, 13969–13985, https://doi.org/10.5194/acp-18-13969-2018, 2018.

Serdyuchenko, A., Gorshelev, V., Weber, M., Chehade, W., and Burrows, J. P.: High spectral resolution ozone absorption cross-sections – Part 2: temperature dependence, Atmos. Meas. Tech., 7, 625–636, https://doi.org/10.5194/amt-7-625-2014, 2014.

Song, Y., Xue, C., Zhang, Y., Liu, P., Bao, F., Li, X., and Mu, Y.: Measurement report: exchange fluxes of HONO over agricultural fields in the North China Plain, Atmos. Chem. Phys., 23, 15733–15747, https://doi.org/10.5194/acp-23-15733-2023, 2023.

Spataro, F. and Ianniello, A.: Sources of atmospheric nitrous acid: state of the science, current research needs, and future prospects, J. Air Waste Manage. Assoc., 64, 1232–1250, https://doi.org/10.1080/10962247.2014.952846, 2014.

Stein, A. F., Draxler, R. R., Rolph, G. D., Stunder, B. J. B., Cohen, M. D., and Ngan, F.: NOAA's HYSPLIT atmospheric transport and dispersion modeling system, B. Am. Meteorol. Soc., 96, 2059–2077, https://doi.org/10.1175/BAMS-D-14-00110.1, 2015.

Stemmler, K., Ammann, M., Donders, C., Kleffmann, J., and George, C.: Photosensitized reduction of nitrogen dioxide on humic acid as a source of nitrous acid, Nature, 440, 195–198, https://doi.org/10.1038/nature04603, 2006.

Stemmler, K., Ndour, M., Elshorbany, Y., Kleffmann, J., D'Anna, B., George, C., Bohn, B., and Ammann, M.: Light induced conversion of nitrogen dioxide into nitrous acid on submicron humic acid aerosol, Atmos. Chem. Phys., 7, 4237–4248, https://doi.org/10.5194/acp-7-4237-2007, 2007.

Stutz, J., Kim, E. S., Platt, U., Bruno, P., Perrino, C., and Febo, A.: UV-visible absorption cross sections of nitrous acid, J. Geophys. Res.-Atmos., 105, 14585–14592, https://doi.org/10.1029/2000JD900003, 2000.

Su, H., Cheng, Y. F., Oswald, R., Behrendt, T., Trebs, I., Meixner, F. X., Andreae, M. O., Cheng, P., Zhang, Y., and Pöschl, U.: Soil nitrite as a source of atmospheric HONO and OH radicals, Science, 333, 1616–1618, https://doi.org/10.1126/science.1207687, 2011.

https://doi.org/10.5194/egusphere-2026-4334
Preprint. Discussion started: 18 August 2026

Tian, X., Wang, Y., Beirle, S., Xie, P., Wagner, T., Xu, J., Li, A., Dörner, S., Ren, B., and Li, X.: Technical note: evaluation of profile retrievals of aerosols and trace gases for MAX-DOAS measurements under different aerosol scenarios based on radiative transfer simulations, Atmos. Chem. Phys., 21, 12867–12894, https://doi.org/10.5194/acp-21-12867-2021, 2021.

Vandaele, A. C., Hermans, C., Simon, P. C., Carleer, M., Colin, R., Fally, S., Mérienne, M.-F., Jenouvrier, A., and Coquart, B.: Measurements of the NO_2 absorption cross-section from 42 000 cm^{-1} to 10 000 cm^{-1} (238–1000 nm) at 220 and 294 K, J. Quant. Spectrosc. Ra., 59, 171–184, https://doi.org/10.1016/S0022-4073(97)00168-4, 1998.

VandenBoer, T. C., Brown, S. S., Murphy, J. G., Keene, W. C., Young, C. J., Pszenny, A. A. P., Kim, S., Warneke, C., de Gouw, J. A., Maben, J. R., Wagner, N. L., Riedel, T. P., Thornton, J. A., Wolfe, D. E., Dubé, W. P., Öztürk, F., Brock, C. A., Grossberg, N., Lefer, B., Lerner, B., Middlebrook, A., and Roberts, J. M.: Understanding the role of the ground surface in HONO vertical structure: high-resolution vertical profiles during NACHTT-11, J. Geophys. Res.-Atmos., 118, 10155–10171, https://doi.org/10.1002/jgrd.50721, 2013.

VandenBoer, T. C., Marković, M. Z., Sanders, J. E., Ren, X., Pusede, S. E., Browne, E. C., Cohen, R. C., Zhang, L., Thomas, J., Brune, W. H., and Murphy, J. G.: Evidence for a nitrous acid (HONO) reservoir at the ground surface in Bakersfield, CA, during CalNex 2010, J. Geophys. Res.-Atmos., 119, 9093–9106, https://doi.org/10.1002/2013JD020971, 2014.

Wang, Y. Q.: MeteoInfo: GIS software for meteorological data visualization and analysis, Meteorol. Appl., 21, 360–368, https://doi.org/10.1002/met.1345, 2014.

Wang, Y., Dörner, S., Donner, S., Böhnke, S., De Smedt, I., Dickerson, R. R., Dong, Z., He, H., Li, Z., Li, Z., Li, D., Liu, D., Ren, X., Theys, N., Wang, Y., Wang, Y., Wang, Z., Xu, H., Xu, J., and Wagner, T.: Vertical profiles of NO2, SO2, HONO, HCHO, CHOCHO and aerosols derived from MAX-DOAS measurements at a rural site in the central western North China Plain and their relation to emission sources and effects of regional transport, Atmos. Chem. Phys., 19, 5417–5449, https://doi.org/10.5194/acp-19-5417-2019, 2019.

Wang, Y., Fu, X., Wu, D., Wang, M., Lu, K., Mu, Y., Liu, Z., Zhang, Y., and Wang, T.: Agricultural fertilization aggravates air pollution by stimulating soil nitrous acid emissions at high soil moisture, Environ. Sci. Technol., 55, 14556–14566, https://doi.org/10.1021/acs.est.1c04134, 2021.

Wang, Y., Lampel, J., Xie, P., Beirle, S., Li, A., Wu, D., and Wagner, T.: Ground-based MAX-DOAS observations of tropospheric aerosols, NO_2, SO_2 and HCHO in Wuxi, China, from 2011 to 2014, Atmos. Chem. Phys., 17, 2189–2215, https://doi.org/10.5194/acp-17-2189-2017, 2017.

Wang, Y., Li, A., Xie, P.-H., Chen, H., Xu, J., Wu, F.-C., Liu, J.-G., and Liu, W.-Q.: Retrieving vertical profile of aerosol extinction by multi-axis differential optical absorption spectroscopy, Acta Phys. Sin., 62, 180705, https://doi.org/10.7498/aps.62.180705, 2013.

Wang, Y., Li, Q., Wang, Y., Ren, C., Saiz-Lopez, A., Xue, L., and Wang, T.: Increasing soil nitrous acid emissions driven by climate and fertilization change aggravate global ozone pollution, Nat. Commun., 16, 2463, https://doi.org/10.1038/s41467-025-57161-6, 2025.

https://doi.org/10.5194/egusphere-2026-4334
Preprint. Discussion started: 18 August 2026

Wang, Y. Q., Zhang, X. Y., and Draxler, R. R.: TrajStat: GIS-based software that uses various trajectory statistical analysis methods to identify potential sources from long-term air pollution measurement data, Environ. Modell. Softw., 24, 938–939, https://doi.org/10.1016/j.envsoft.2009.01.004, 2009.

Wong, K. W., Oh, H.-J., Lefer, B. L., Rappenglück, B., and Stutz, J.: Vertical profiles of nitrous acid in the nocturnal urban atmosphere of Houston, TX, Atmos. Chem. Phys., 11, 3595–3609, https://doi.org/10.5194/acp-11-3595-2011, 2011.

Wong, K. W., Tsai, C., Lefer, B., Grossberg, N., and Stutz, J.: Modeling of daytime HONO vertical gradients during SHARP 2009, Atmos. Chem. Phys., 13, 3587–3601, https://doi.org/10.5194/acp-13-3587-2013, 2013.

Xing, C., Liu, C., Li, Q., Wang, S., Tan, W., Zou, T., Wang, Z., and Lu, C.: Observations of HONO and its precursors between urban and its surrounding agricultural fields: the vertical transports, sources and contribution to OH, Sci. Total Environ., 915, 169159, https://doi.org/10.1016/j.scitotenv.2023.169159, 2024.

Xing, C., Xu, S., Song, Y., Liu, C., Liu, Y., Lu, K., Tan, W., Zhang, C., Hu, Q., Wang, S., Wu, H., and Lin, H.: A new insight into the vertical differences in NO_2 heterogeneous reaction to produce HONO over inland and marginal seas, Atmos. Chem. Phys., 23, 5815–5834, https://doi.org/10.5194/acp-23-5815-2023, 2023.

Ye, C., Lu, K., Ma, X., Qiu, W., Li, S., Yang, X., Xue, C., Zhai, T., Liu, Y., Li, X., Li, Y., Wang, H., Tan, Z., Chen, X., Dong, H., Zeng, L., Hu, M., and Zhang, Y.: HONO chemistry at a suburban site during the EXPLORE-YRD campaign in 2018: formation mechanisms and impacts on O_3 production, Atmos. Chem. Phys., 23, 15455–15472, https://doi.org/10.5194/acp-23-15455-2023, 2023.

Ye, C., Zhang, N., Gao, H., and Zhou, X.: Photolysis of particulate nitrate as a source of HONO and NO_x, Environ. Sci. Technol., 51, 6849–6856, https://doi.org/10.1021/acs.est.7b00387, 2017.

Zhang, J., Duan, Z., Zhou, S., Li, Y., and Gao, Z.: Gap filling of turbulent heat fluxes over rice–wheat rotation croplands using the random forest model, Atmos. Meas. Tech., 16, 2197–2207, https://doi.org/10.5194/amt-16-2197-2023, 2023.

Zhang, J., Lian, C., Wang, W., Ge, M., Guo, Y., Ran, H., Zhang, Y., Zheng, F., Fan, X., Yan, C., Daellenbach, K. R., Liu, Y., Kulmala, M., and An, J.: Amplified role of potential HONO sources in O_3 formation in North China Plain during autumn haze aggravating processes, Atmos. Chem. Phys., 22, 3275–3302, https://doi.org/10.5194/acp-22-3275-2022, 2022.

Zhou, X., Gao, H., He, Y., Huang, G., Bertman, S. B., Civerolo, K., and Schwab, J.: Nitric acid photolysis on surfaces in low-NO_x environments: significant atmospheric implications, Geophys. Res. Lett., 30, 2217, https://doi.org/10.1029/2003GL018620, 2003.